

Actin cytoskeleton promotes Nipah virus assembly by regulating the  
nanoscale organization of the matrix protein

Vicky Kliemke

Institute of Parasitology

McGill University

Montréal, Quebec, Canada

September 2023

A thesis submitted to McGill University in partial fulfillment of the requirements of the degree of  
Master of Science

© Vicky Kliemke (2023)

## Table of Contents

Table of contents .....	2
Acknowledgements .....	4
Contribution of authors .....	5
Abbreviations .....	6
List of figures .....	8
Abstract .....	9
Résumé .....	10
1. Introduction.....	12
1.1 The Paramyxoviridae; important agents of disease .....	12
1.2 The life cycle of Henipaviruses .....	18
1.3 Nipah virus Matrix protein role in assembly and budding .....	20
1.4 The actin cytoskeleton in virus assembly and budding .....	23
1.5 Using single-molecule localization microscopy to resolve the organization of NiV-M proteins .....	25
2. Project overview .....	28
2.1 Rationale and Hypothesis .....	28
2.2 Specific aims .....	29
3. Methodology.....	30
3.1 Cell culture.....	30
3.2 Expression plasmids .....	30
3.3 PCR.....	31
3.4 Cell seeding & Transfection of plasmids.....	32
3.5 Immunofluorescence for SMLM .....	33
3.6 LatA and DMSO treatment.....	33
3.7 SMLM set-up.....	33
3.8 SMLM image acquisition and reconstruction.....	34
3.9 Western blot for VLP budding assay.....	35
3.10 VLP production and Cell lysate preparation.....	36
3.11 Statistical analysis.....	36

3.12 VLP budding assay .....	37
3.13 Immunofluorescence for confocal microscopy.....	37
3.14 Co-Immunoprecipitation.....	39
3.15 Nipah matrix structure .....	40
4. Results.....	41
4.1 NiV-M possesses a PxxP and KLKK like motif shared among some paramyxoviruses and actin binding proteins.....	41
4.2 Mutagenesis studies of PxxP and KLKK-like motif .....	44
4.3 A putative actin-binding domain at NiV-M is key for virus budding and actin incorporation in VLPs.....	49
4.4 Mutations at the putative actin-binding domain in NiV-M alter the nanoscale organization of NiV-M. ....	52
4.5 Latrunculin A alters the nanoscale organization of NiV-M .....	60
5. Discussion .....	66
5.1 The role of the putative actin-binding motif in NiV-M on virus assembly via actin interaction .....	66
5.2 Comparing Isoleucine 349 and Lysine 351 in Actin Binding and Interaction .....	67
5.3 Analyzing Latrunculin A (LatA) Effects on NiV-M-Actin Association .....	68
5.4 The Actin cytoskeleton and NiV-M: Avenues for Further Research .....	69
5.5 Targeting the NiV-M-Actin Interaction for New Antiviral Therapies .....	71
5.6 Our Discovery of the PxxP Motif and Its Significance in Paramyxovirus Biology .....	71
5.7 Understanding the Role of the PxxP Motif in Budding.....	72
6. Conclusion .....	74
7. References .....	76

## **Acknowledgments**

Firstly, I would like to thank my supervisor Dr. Liu for providing me with an invaluable opportunity to work in her lab and for her guidance and mentorship throughout my time there. Dr. Liu's belief in my potential has been a driving force behind my growth and development. I extend my sincere appreciation to the entire lab team for creating an environment of support, camaraderie, and intellectual stimulation. Special thanks go to Qian Wang and Yuhang Luo for their invaluable teachings, which have greatly enriched my understanding and skills. I am deeply thankful for the invaluable feedback provided by my esteemed committee members, Dr. Arnold Heyer and Dr. Andrew Mouland, during my committee meeting. I am grateful to Dr. Thavy Long for giving me the opportunity to contribute to the Scientific Outreach Program. This role not only enabled me to refine my oral communication skills across diverse age groups but also allowed me to engage with various audiences. My appreciation extends to Dr. Youssef Chebli for his incredible support and exceptional guidance. His expertise in multiple imaging techniques and his willingness to address all my questions have been invaluable assets to my learning. I am truly honored to have been the recipient of the Lynden Laird Lyster Memorial Fellowship in Parasitology, awarded by the esteemed members of the Parasitology Institute. I would also like to extend my heartfelt gratitude to the entire Institute of Parasitology community for fostering an environment of excellence, collaboration, and shared learning, which has significantly contributed to my academic journey. In conclusion, I am immensely thankful to each individual mentioned here for their contributions to my academic and personal growth. Their collective support has paved the way for my achievements, and I am eager to carry these lessons forward in my future endeavors.

Vicky Kliemke

### **Contribution of authors**

The manuscript was authored by Vicky Kliemke, with subsequent revisions and corrections overseen by my supervisor, Dr. Liu. The experiments and data analysis detailed in this manuscript were conducted by Vicky Kliemke, with assistance and guidance provided by Dr. Liu.

**Abbreviations:**

PM : plasma membrane

NiV : Nipah

NiV-M : Nipah matrix protein

HN : hemagglutinin-neuraminidase

G: glycoproteins

H: hemagglutinin

RNA: ribonucleic acid

N: nucleoprotein

P : phosphoprotein

VLP: virus-like particles

PI(4,5)P2: Phosphatidylinositol-4,5-bisphosphate

MeV: Measles virus

SeV : Sendai virus

MuV : Mumps virus

NDV: Newcastle disease virus

SMLM: single-molecule localization microscopy

PSF: point spread function

DBSCAN: Density-Based Spatial Clustering of Applications with Noise

TIRF: total internal reflection fluorescence

HEK293T: Human kidney epithelial cell

PK13: Pig Kidney cells

DMEM: Dulbecco's Modified Eagle's Medium

FBS: Fetal Bovine Serum

PBS: phosphate buffered saline

GFP: Green fluorescent protein

PFA: paraformaldehyde

DMSO: dimethyl sulfoxide

LatA: Latrunculin A

MEA: mercaptoethylamine

BME:  $\beta$ -mercaptoethanol

PVDF: polyvinylidene difluoride

EDTA: ethylenediaminetetraacetic acid

PEI: Polyethylenimine

GAPDH: Glyceraldehyde 3-phosphate dehydrogenase

Hpiv-1: Human parainfluenza virus

WASP: Wiskott-Alderich syndrome protein

WASF2: WASP family member 2

ROI: region of interest

TAD: total average density

WT: Wild-type

SH3: SRC Homology 3

ESCRT: endosomal sorting complexes required for transport

HIV: human immunodeficiency virus

HPV: Human Papillomavirus

## List of figures:

<b>Figure 1.</b> Paramyxovirus phylogenetic tree based on the polymerase protein.....	p.13
<b>Figure 2.</b> Paramyxovirus life cycle.....	p.14
<b>Figure 3.</b> Pteropus Bats geographical range and Nipah virus outbreaks.....	p.16
<b>Figure 4.</b> Nipah virus transmission modes.....	p.19
<b>Figure 5.</b> Nipah matrix protein crystal structure.....	p.20
<b>Figure 6.</b> NiV-M creating local curvature at the plasma membrane.....	p.21
<b>Figure 7.</b> M protein forming a matrix array.....	p.22
<b>Figure 8.</b> Actin cytoskeleton role in assembly and budding of Paramyxoviruses.....	p.24
<b>Figure 9.</b> Single-molecule localization microscopy.....	p.27
<b>Figure 10.</b> NiV-M sequence alignment with SeV-M, hPIV1-M, and actin-binding proteins...	p.42
<b>Figure 11.</b> The PxxP and KLKK-like motifs do not hinder membrane association or dimerization.....	p.43
<b>Figure 12.</b> Mutagenesis of PxxP and KLKK-like motifs.....	p.44
<b>Figure 13.</b> Functionality of the mutants created by comparing cellular lysate and VLP expression.....	p.47
<b>Figure 14.</b> Actin incorporation in NiV-M VLPs.....	p.50
<b>Fig. 15.</b> The nano-organization NiV-M mutants within the KLKK-like motif show a different cluster pattern than WT.....	p.54
<b>Figure 16:</b> The I349A mutation alters the nanoscale organization of NiV-M on the plasma membrane.....	p.58
<b>Figure 17:</b> The nano-organization of LatA-treated cells displays a distinct cluster pattern compared to control cells treated with DMSO.....	p.61
<b>Figure 18:</b> LatA alters the nanoscale organization of NiV-M on the plasma membrane similarly to I349A.....	p.64

**Abstract.** The Paramyxovirus family includes a range of highly infectious and pathogenic viruses that cause severe diseases in animals and humans. Their matrix protein (M) plays a crucial role in the late stages of the viral lifecycle, responsible for assembly and budding. The assembly and budding processes of M proteins take place at the host cell plasma membrane. M proteins form dimers, localize to the plasma membrane by binding to the inner leaflet, and subsequently assemble into a matrix array, generating membrane curvature for budding. The nanometer-scale investigation of these M arrays at the plasma membrane remains unexplored, leaving several inquiries unanswered such as how these are formed. Here, we use Nipah virus, a deadly zoonotic paramyxovirus as a model to study the nano-organization of M at the plasma membrane. This virus was chosen because there are no approved therapeutics or vaccines for it, and it ranks among the top ten threats according to the World Health Organization (WHO). Additionally, NiV has a high mortality rate, causing annual human encephalitis outbreaks in Southeast Asia with a mortality rate exceeding 75%. Since many paramyxoviruses have been found to exploit the actin cytoskeleton, we investigated if the actin cytoskeleton is involved in the assembly process of NiV. Using single-molecule localization microscopy, we quantified the organization of the NiV-M assembly sites on a nanoscale at the PM to study the role of actin cytoskeleton in regulating the nano-organization of these NiV-M assembly sites. We identified a KLKK-like motif at the C-terminus of NiV-M, present in numerous actin-binding proteins. Mutations in this motif within NiV-M lead to decreased actin-NiV-M interactions and resulted in reduced budding. Our single-molecule imaging data reveals that NiV-M constructs carrying mutations in the C-terminal KLKK-like motif exhibit lower molecular density and smaller NiV-M assemblies on the plasma membrane. Altogether, the interaction between NiV-M and actin facilitates the formation of large M arrays, priming them for budding. My findings provide novel insights on the NiV assembly mechanism and reveal novel targets for antiviral therapeutics development.

**Résumé.** La famille des Paramyxovirus comprend une variété de virus hautement infectieux et pathogènes qui provoquent des maladies graves chez les animaux et les humains. Leur protéine matrice (M) joue un rôle crucial dans les dernières étapes du cycle de vie viral, responsable de l'assemblage et du bourgeonnement du virus. Cette caractéristique rend la protéine M une cible attrayante pour l'intervention antivirale. Les processus d'assemblage et de bourgeonnement des protéines M ont lieu à la membrane plasmique de la cellule hôte. Les protéines M forment des dimères, se localisent à la membrane plasmique interne, puis s'assemblent en une matrice à la membrane plasmique, générant une courbure membranaire pour le bourgeonnement. Cependant, de nombreuses questions demeurent non résolues concernant ce processus. L'investigation à l'échelle nanométrique de ces matrices M à la membrane plasmique reste inexplorée, laissant plusieurs questions sans réponse, comme leur formation. Ici, nous utiliserons le virus Nipah, un paramyxovirus zoonotique mortel, comme modèle pour étudier la nano-organisation de la protéine M à la membrane plasmique. Ce virus a été choisi car il n'existe pas de traitements ou de vaccins approuvés, et il figure parmi les dix principales menaces selon l'Organisation Mondiale de la santé (OMS). De plus, le NiV a un taux de mortalité élevé, provoquant des épidémies annuelles d'encéphalite humaine en Asie du Sud-Est avec un taux de mortalité dépassant 75 %. Étant donné que de nombreux paramyxovirus ont été trouvés exploitant le cytosquelette d'actine, nous avons étudié si le cytosquelette d'actine est impliqué dans le processus d'assemblage du NiV. En utilisant la microscopie de localisation de molécule unique, nous avons quantifié l'organisation des sites d'assemblage NiV-M à une échelle nanométrique à la membrane plasmique pour étudier le rôle du cytosquelette d'actine dans la régulation de la nano-organisation de ces sites d'assemblage NiV-M. Nous avons identifié un motif similaire à KLKK à l'extrémité C-terminale de NiV-M, présent dans de nombreuses protéines de liaison à l'actine. Les mutations dans ce motif au sein de NiV-M entraînent des interactions actine-NiV-M réduites et entraînent

un bourgeonnement réduit. Nos données d'imagerie à molécule unique révèlent que les constructions NiV-M portant des mutations dans le motif similaire à KLKK à l'extrémité C-terminale présentent une densité moléculaire réduite et des assemblages NiV-M plus petits à la membrane plasmique. Dans l'ensemble, l'interaction entre NiV-M et l'actine facilite la formation de grandes matrices M, les préparant au bourgeonnement.

## 1. Introduction

### 1.1. The Paramyxoviruses are important agents of disease.

The paramyxovirus family encompasses a range of important pathogens affecting both animals and humans, including canine distemper, mumps, Newcastle disease, and Nipah viruses, among others (*Figure 1*) [1]. Among them, some paramyxoviruses have been circulating in human populations for centuries. For example, the measles virus (MeV), a highly contagious airborne virus, caused approximately 128,000 deaths globally among unvaccinated or young children in 2021 [2]. In contrast, other paramyxoviruses, such as Hendra virus (HeV) and Nipah virus (NiV), have emerged more recently [3].

The emergence of novel zoonotic paramyxoviruses, which are diseases that can be transmitted from animals to humans, poses a significant threat and risk for the potential development of future pandemics. Despite the comprehensive sequencing and cataloging of many new paramyxoviruses, there might be other paramyxovirus genera present in bats or other reservoirs that remain undiscovered but still possess the potential to spill over to humans [3]. In a landmark study, researchers identified over 66 novel paramyxoviruses in bats and rodents from various locations globally, suggesting their potency in switching between hosts, including bats, mammals, and birds [4].

The Henipaviruses, being highly lethal emerging viruses, have been discovered more recently. The Henipavirus genus, comprising Nipah and Hendra viruses, are zoonotic viruses within this family, naturally infecting bats and potentially spilling over to other mammals, notably humans, with significant mortality rates. For instance, Nipah virus has been identified as a major threat by the WHO, causing mortality rates exceeding 70% in Southeast Asia and Australia [1].

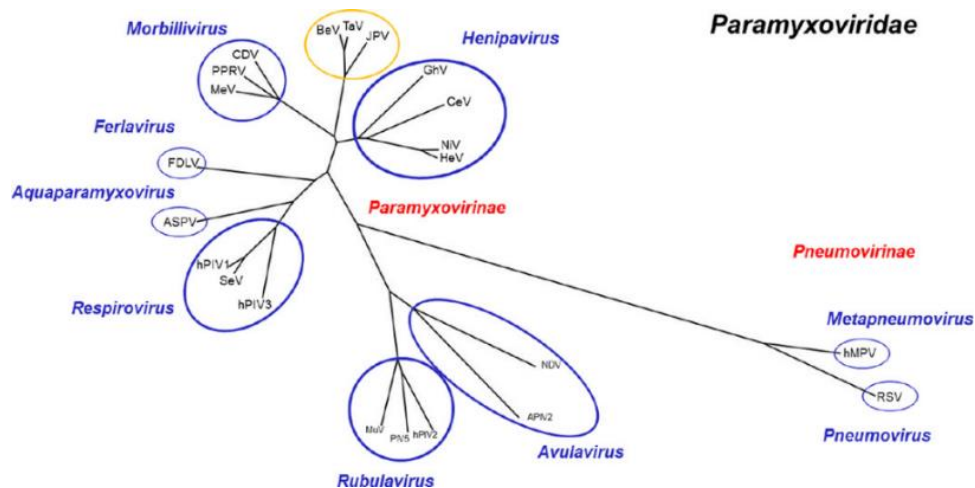


**Figure 1. Paramyxovirus phylogenetic tree based on the polymerase protein.** Large polymerase was used to generate the phylogenetic tree. Sequences from viruses were acquired from the NCBI database [5].

Nipah virus was first characterized in 1999 after a devastating outbreak in Malaysia, resulting in 300 human cases and leading to the culling of more than 1 million pigs, nearly decimating the pork industry. Most individuals infected with Nipah virus develop acute encephalitis and respiratory illness, with a high mortality rate. The fruit bat species in the genus *Pteropus*, family Pteropodidae, serves as the main reservoir for both Nipah and Hendra viruses, yet these bats do not develop the disease, whether infected naturally or experimentally [6]. Fruit bats have a wide geographical range, putting several countries, including Australia, Bangladesh, India, and Malaysia, at risk (*Figure 2*) [7].

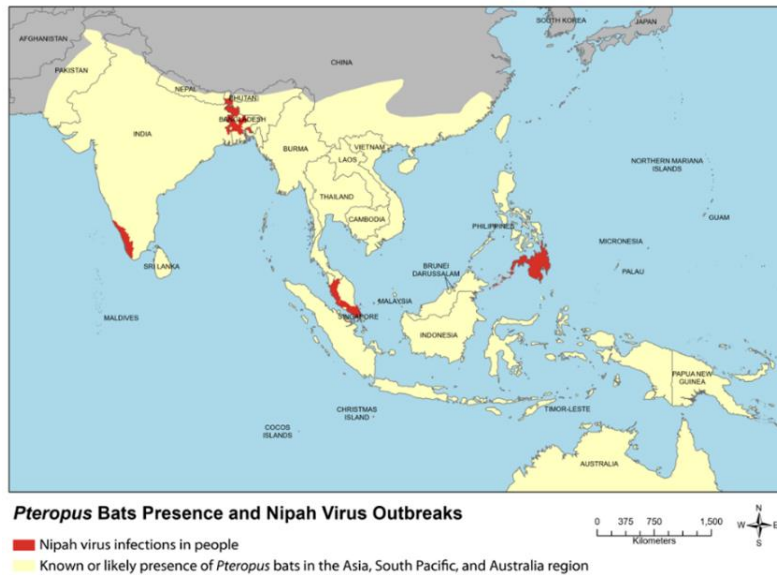


**Figure 2. Pteropus Bats geographical range and Nipah virus outbreaks.** This map displays Nipah outbreaks among people in red, and it indicates the presence of the pteropus bats, which carry the Nipah virus, in yellow[8].

NiV Yearly outbreaks occur in some parts of Asia, with particularly frequent occurrences in India and Bangladesh. Since January 4th of 2023, Bangladesh has reported 10 confirmed cases of Nipah virus, a zoonotic virus that can be transmitted from animals to humans, tragically resulting in 8 fatalities [9]. In the southern state of Kerala, India, an outbreak of Nipah virus infection emerged in late August 2023, affecting 6 individuals, with 2 fatalities. In India, an intensive testing initiative involving over 700 individuals, including healthcare workers, has been underway over the past week to limit further virus spread. In response to this critical situation, the state has taken significant measures, including the closure of schools, offices, and the suspension of public transport services [10]. Nipah virus outbreaks have been a recurring concern in Kerala over the past 5 years, beginning in 2018 with 17 deaths and 18 confirmed cases. The fatality rates have ranged from 40% to 75%, depending on the strain [10,11]. Unfortunately, no therapeutic treatment or vaccine for Nipah virus is available, making it one of the top 10 priorities of the

WHO. As of now, supportive care and preventive measures are the only recourse against this deadly virus [12].

Transmission of Nipah virus can occur through multiple routes, including animal-to-animal, human-to-human, and animal-to-human. Specifically, transmission may result from direct contact with infected animals, such as pigs or bats, or their body fluids. Consumption of infected animals or products contaminated by body fluids can lead to infection. Close contact with an individual infected with Nipah virus or their body fluids, including nasal secretions, respiratory droplets, urine, or blood, also poses a transmission risk (*Figure 3*) [13,14]. There are many hosts susceptible to Nipah, as the entry receptor ephrinB2/B3 is shared among many mammals. The virus can naturally infect pigs, horses, dogs, cats, humans, and possibly many other species [7]. In humans, transmission primarily occurs through the oronasopharyngeal route, with the initial infection taking place in the respiratory mucosa. The virus's high replication capacity enables viral particles to reach distant tissues beyond the site of the initial infection. Eventually, the virus migrates to the endothelial cells of the central nervous system, leading to the development of encephalitis [15].

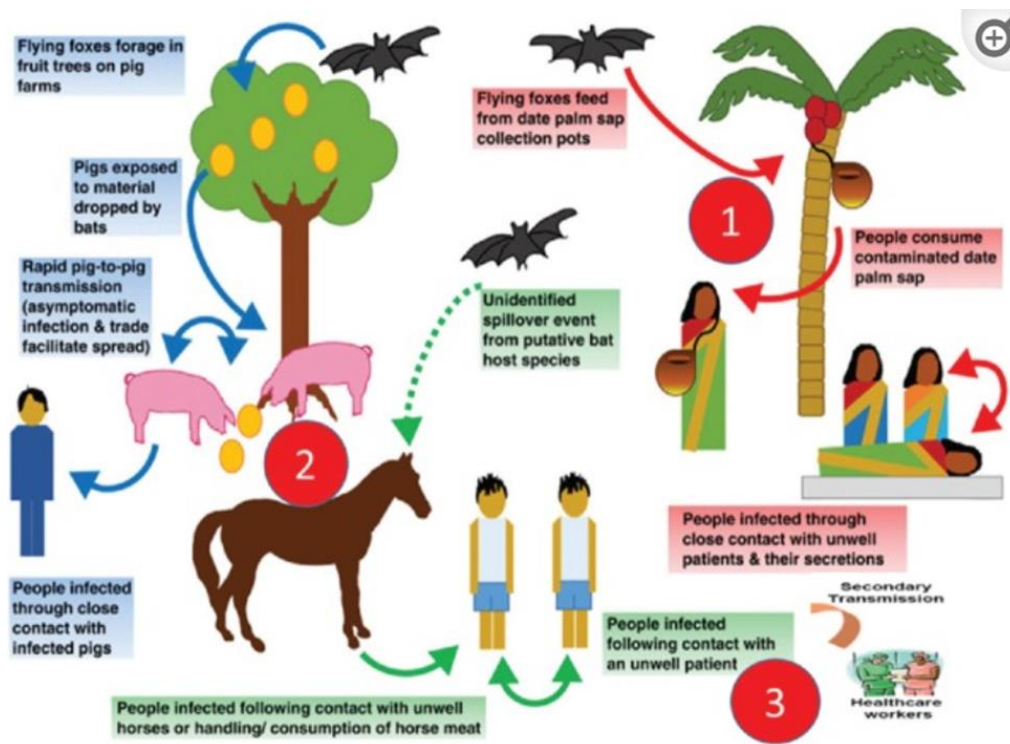


**Figure 3. Nipah virus transmission modes.** Fruit bats are known to consume palm sap and can contaminate it through contact with their saliva, urine, or feces. In some countries, the consumption of fresh palm sap is a popular practice. However, if this sap becomes contaminated, it can lead to infections in humans (1). Human-to-human transmission has been observed during outbreaks, such as in India, where healthcare workers became infected from their patients, resulting in nosocomial infections (3). Domesticated animals, like pigs and horses living on farms, can also be exposed to bat saliva, feces, or urine, especially if there are fruit trees on the farms (2). Close contact with infected domesticated animals can lead to Nipah virus (NiV) infection (1). NiV is highly contagious among pigs and can be spread through respiratory droplets, including coughing (2). In summary, transmission of Nipah virus can occur through multiple routes, including animal-to-human (1), animal-to-animal (2) and human-to-human (3) [14].

Regarding the clinical presentation of Nipah virus, its incubation period ranges from 4 days to 2 months, with approximately 90% of cases displaying symptoms within 2 weeks. Patients initially experience fever, headache, and vomiting, progressing to more severe symptoms like encephalitis, brainstem dysfunction, seizures, and vasomotor changes. Nipah is well-documented for causing neurological diseases, but it can also affect different organs to varying degrees [7].

## 1.2 The life cycle of Henipaviruses.

At a molecular level, paramyxoviruses are non-segmented negative-stranded RNA genome enveloped viruses. In the case of Henipavirus, the viral membrane bears the fusion (F) and glycoprotein (G). The G attachment binds to the protein receptors and upon initial attachment to the ephrinB2/B3 receptor, the G proteins induce a conformational change in the fusion protein (F), enabling virus entry into the host cell. Most paramyxoviruses enter the host cell through fusion between the host cell plasma membrane and the viral membrane, releasing the nucleocapsid containing the viral genome into the cell's cytosol. Once a cell is infected, multiple F and G proteins are expressed on its cellular surface, enabling membrane fusion interaction with neighbouring cells bearing the cellular receptor. This leads to the formation of multi-nucleated cells (syncytia), a hallmark of paramyxovirus infection. Once inside the host cell, the paramyxovirus genome undergoes replication. The viral RNA-dependent RNA polymerase encoded by the L gene (L) transcribes the single-stranded negative-sense RNA (-ssRNA) from the 3-prime end to the 5-prime end, producing positive-sense RNA. This mRNA can then be translated and replicated by the host cellular machinery. The viral genome also encodes a nucleoprotein (N), which binds to the RNA genome, safeguarding it from degradation. Furthermore, the P gene (phosphoprotein) encodes the V, W, and C proteins, playing a crucial role in modulating the innate immune response. Finally, the matrix protein (M) orchestrates the assembly and budding of the virus, incorporating all six proteins; N (nucleocapsid), M (matrix), L (polymerase), P (phosphoprotein), F (fusion), and G (glycoprotein) into the virion (*Figure 4*) [16,17].

Given the crucial role of the M protein in orchestrating the assembly and budding processes at the host cell's plasma membrane, it emerges as a promising target for antiviral strategies [15].

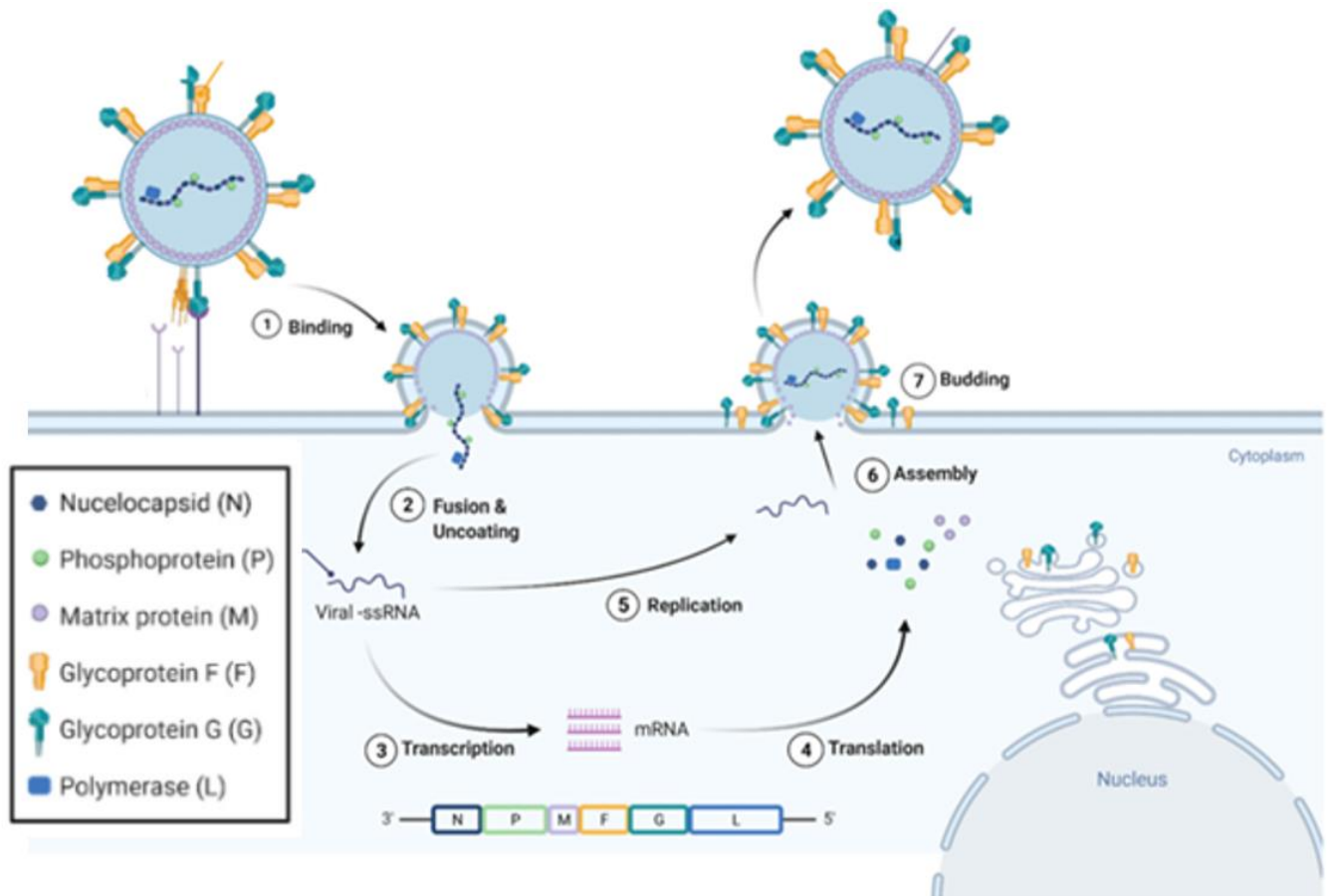


**Figure 4. Paramyxovirus life cycle.** The Nipah virus G protein attaches to the ephrinB2/B3 receptor (1), leading to the release of the viral genome into the cytoplasm (2). The negative-sense single-stranded RNA (-ssRNA) is transcribed (3) into mRNA, initiating the translation of viral proteins including N (nucleocapsid), M (matrix), L (polymerase), P (phosphoprotein), F (fusion), and G (glycoprotein) (4). Subsequently, the positive-sense single-stranded RNA (ssRNA) is replicated (5) for incorporation into the virion at the plasma membrane. At the plasma membrane, all viral proteins undergo assembly (6), resulting in the formation of a complete virion that eventually buds off from the host cell (7) [18].

### 1.3 Nipah virus Matrix protein role in assembly and budding.

The M protein plays a crucial role in orchestrating the assembly and budding process at the host cell's plasma membrane. The monomeric M protein assembles into dimers whose crystal structure revealed recently (*Figure 5*) [19]. NiV-M alone can generate virus-like particles (VLPs). These VLPs resemble virus particles but lack genetic material, rendering them incapable of infecting host cells [20].

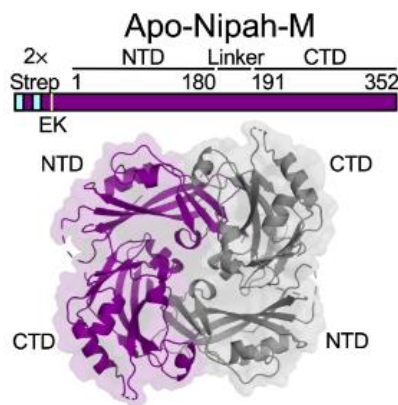


**Figure 5. Nipah matrix protein crystal structure.** Crystal structure of NiV-M dimers (purple and gray). The protein domains, N-terminal domain (NTD), linker, and C-terminal domain (CTD) are outlined [19].

NiV-M proteins assemble at the plasma membrane and localize to the inner leaflet through nonspecific electrostatic interactions facilitated by basic patches found on the M protein. Once localized at the plasma membrane, the M protein needs to anchor itself to the inner leaflet, and it achieves this by binding to Phosphatidylinositol-4,5-bisphosphate PI(4,5)P2 [19]. The interaction between M and PI(4,5)P2 causes a conformational change in M leading to the positively charged basic patches on the side of the protein to expose negatively charged patches in the center of the donut-shaped protein. Consequently, this generates repulsion between the negatively charged

inner leaflet of the plasma membrane and the negatively charged patches in the center of the M protein, leading to localized membrane curvature [19]. In summary, it can assemble into dimers, localizes at the inner leaflet of the plasma membrane through non-specific electrostatic interactions, and drives outward local curvature (*Figure 6*) [19].

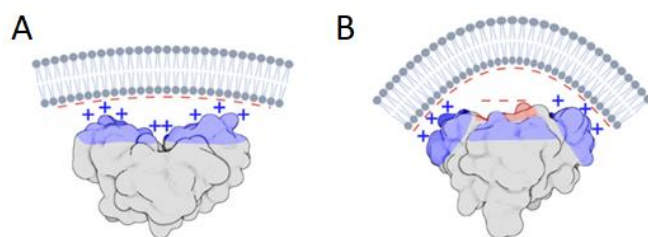


**Figure 6. NiV-M creating local curvature at the plasma membrane.** Model of NiV-M protein dimer binding to the inner leaflet of the plasma membrane through electrostatic interactions (A). M bound PI(4,5)P2 causes a conformational change in M leading to the positively charged basic patches on the side of the protein to expose negatively charged patches in the center of the protein thus leading to repulsion forcing upward membrane curvature (B) [19].

Moreover, recent research has demonstrated that the Measles virus (MeV) M protein, during the course of infection, can undergo further organization into a matrix array, as evidenced by cryoelectron tomography (*Figure 7*). These intricate lattices underlie the plasma membrane of infected cells and are believed to play a crucial role in the virion assembly process. It is believed that these MeV-M lattices serve as bridges between the viral glycoproteins and the internal ribonucleocapsid containing the genetic material of the virions. Consequently, the MeV-M exhibit the capacity to form a two-dimensional paracrystalline array with the membrane, shedding new light on their sub-nanometer organizational structure [21]. Nevertheless, the nanometer-scale investigation of these NiV-M arrays at the plasma membrane remains unexplored, leaving several

inquiries unanswered. One such question pertains to the mechanism underlying the formation of these substantial lattices [19]. One possibility is that NiV-M is interacting with host cellular machinery for its assembly and budding. Since many paramyxoviruses hijack the cellular machinery to accomplish budding, we think that cellular proteins such as actin cytoskeleton could be involved in assembly stage and budding of Nipah virus [22].

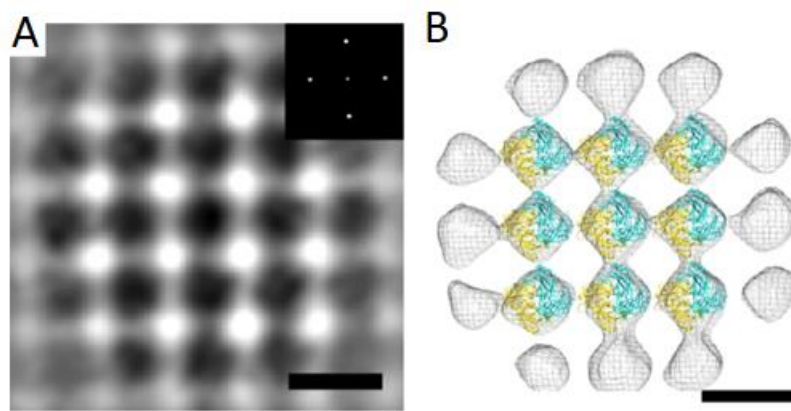


**Figure 7. M protein forming a matrix array.** Cryo-electron tomography of MeV-M lattice and tomographic slice enhanced to improve protein structure (A). Model depicting monomer arrangements of MeV shown in cyan and yellow (B) [21].

#### **1.4. The actin cytoskeleton in virus assembly and budding.**

Numerous viruses are known to hijack the actin cytoskeleton and use it to their advantage. Paramyxoviruses have been shown to interact with the actin cytoskeleton, a connection dating back to the 1970s when cellular actin was isolated from MeV preparations [23]. Subsequent electron microscopic studies revealed MeV budding from microvillus-like structures that contained actin (*Figure 8*) [24]. Further support for this interaction emerged through the use of cytochalasin B, a metabolite known to block actin polymerization and elongation. Inhibition of actin filament elongation inhibited the budding of MeV [25]. Extending beyond MeV, multiple investigations demonstrated actin reorganization in various paramyxoviruses from different genera—MeV, Mumps (MuV), Sendai (SeV), and Newcastle disease virus (NDV) [26]. Certain paramyxoviruses even exhibit direct interactions with purified actin. For instance, both SeV and NDV's M proteins have been shown to directly interact with actin [15]. In the case of SeV, a potential actin binding motif was identified in the C-terminal region of the Matrix protein. The residues crucial for budding shared remarkable similarity with a KLKK-like motif present in various actin-binding proteins. This observation prompted the speculation that this motif might be associated with actin binding. While mutations within this region hindered VLP production, they did not disrupt membrane association [27]. For NiV-M protein, it remains uncertain if it can interact with the actin cytoskeleton in the same manner. A proteomic-based interaction study identified several important actin regulators particularly those involved in cytoskeleton remodeling, such as cofilin and the ARP2/3 complexes, as binding partners for NiV-M protein [22]. Therefore, it is believed that the actin cytoskeleton might play a crucial role for assembly and budding for NiV [15]. Therefore, our research question is whether the actin cytoskeleton regulates the formation of NiV-M arrays on a nanoscale. To answer our research question, we are

using single-molecule localization microscopy to quantify the organization of NiV-M assembly sites on a nanoscale at the plasma membrane.

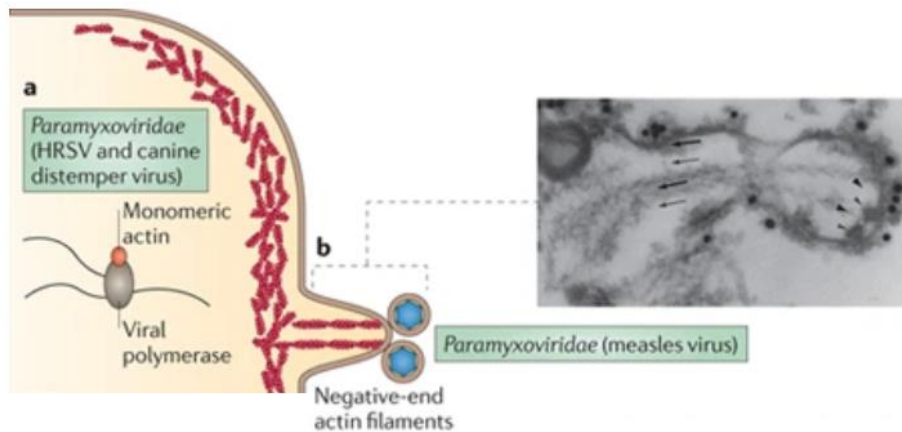


**Figure 8. Actin cytoskeleton role in assembly and budding of Paramyxoviruses.**

Paramyxoviruses Human Respiratory Syncytial virus (HRSV) and canine distemper virus negative-strand RNA associates with actin monomers to stimulate polymerase activity (a).

Measles virus often associates with negative-oriented actin filaments to bud off the plasma membrane (b) [28].

## **1.5. Using single-molecule localization microscopy to resolve the organization of NiV-M proteins.**

In a conventional microscope, optical resolution is limited to half the wavelength of light, resulting in a resolution limit of 200-300 nm. This constraint becomes significant when studying virus-related structures, such as the NiV assembly sites, which range in size from 40 to 500 nm. As a result, the diffraction limit presents a considerable challenge. To gain insights into viral processes, it's crucial to understand how biomolecules are organized at a spatial scale that matches their size. This knowledge not only illuminates biomolecule interactions at the nanometer scale but also holds the potential for informing disease treatments [29].

Single-molecule localization microscopy (SMLM) is a powerful tool that overcomes the limitations of diffraction-limited techniques by enhancing spatial resolution. This advancement allows us to examine biological structures at the nanoscale. SMLM employs conventional wide-field excitation and typically achieves spatial resolutions ranging from 20 to 50 nm using super-resolution techniques applied to individual molecules [29]. Our custom-built single-molecule localization microscope attains a lateral resolution of 10 nm (*Figure 9 B*) [30]. SMLM can detect spatial coordinates of fluorophores (fluorescent molecules) with high precision due to their spatial separation. To prevent fluorophore overlap, they are designed to be photoswitchable, toggling between ON (bright state) and OFF states (dark state) (*Figure 9 A*). Laser irradiation and careful control of the chemical environment dictate this switching. Only a subset of fluorophores is allowed to be in the ON state, ensuring spatially isolated fluorophores. This ON/OFF/ON cycle leads to the blinking phenomenon observed in photoswitchable fluorophores like Alexa Fluor 647 [31].

SMLM detects individual fluorophores by determining the center of point spread function (PSF) [31]. A PSF of an individual fluorophore is around 200 nanometers wide. However, the unique behavior of these molecules allows us to accurately pinpoint their positions with greater precision than the PSF's size [32]. To ensure that the PSF created by individual fluorescent molecules don't overlap, the fluorescent emissions of different molecules are separated in time. This is achieved by taking advantage of photoswitching, which is the most common method used to achieve this temporal separation [31]. Notably, proper irradiation and chemical conditions influence photoswitching. Samples are immersed in an imaging buffer containing thiols like mercaptoethylamine and an enzymatic oxygen scavenger [33].

The super-resolution images are subsequently assembled computationally. Single-molecule localizations depend on pixel regions and are further analyzed into subpixel (x,y) coordinates for each molecule using MATLAB software. For quantitative analysis, clusters are identified, and molecules are counted using a program called Density-Based Spatial Clustering of Applications with Noise (DBSCAN) algorithm [31]. This algorithm can be applied to reconstructed images obtained through SMLM and identifies closely grouped localizations and detects outliers [34].

In addition to enabling quantitative analysis through the DBSCAN algorithm, SMLM opens the door to impactful research in the field of biology [29]. For instance, S. V. Pigeon et al. conducted a study using single-molecule localization microscopy to quantify the clustering pattern of TCR-CD3 complexes on a nanoscale, revealing crucial insights into triggered and nontriggered TCR-CD3 complexes based on their cluster density [35]. Given that NiV-M assembly and budding predominantly occur at the plasma membrane, our research focus centers on imaging the dorsal membrane of cells [30]. To accomplish this, we employ total internal reflection fluorescence (TIRF) microscopy. TIRF microscopy involves directing the laser beam at a steep angle, causing

it to exclusively interact with the coverslip-sample interface. As a result, only a thin layer of the sample, approximately 200 nm in depth, is illuminated. This approach not only reduces background noise but also significantly enhances resolution (*Figure 9 C*) [31].

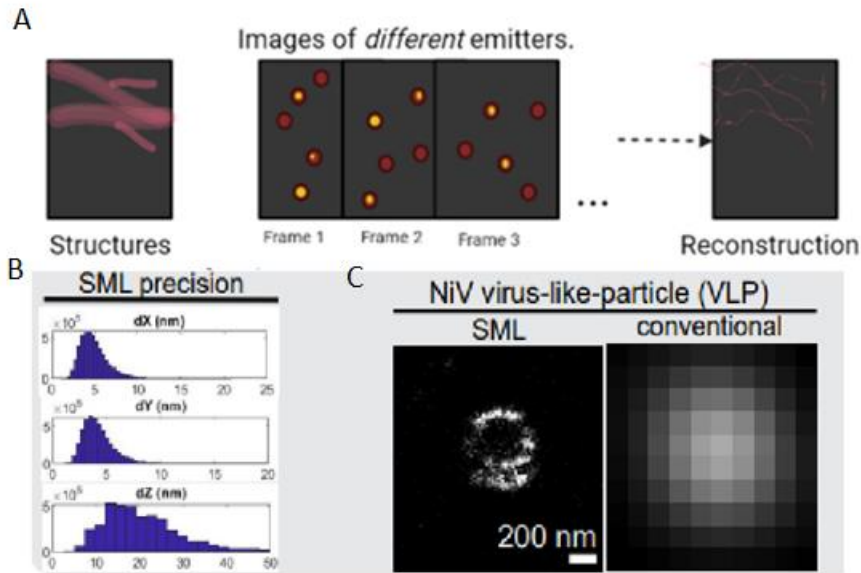


**Figure 9. Single-molecule localization microscopy.** Biomolecular structures can be visualized with greater precision using SML microscopy. The process of photoswitching fluorophores, as depicted in the different frames, allows them to be positioned farther apart in space. This result in improved reconstruction (A). The custom-built SML microscope offers a lateral precision of 10 nm (B). A comparison of Nipah VLP imaging is shown between single-molecule localization microscopy (SMLM) and conventional microscopy. The scale bar measures 200 nm (C) [30,23].

## 2. Project Overview

### 2.1 Rationale and Hypothesis.

It is believed that paramyxovirus M proteins assemble into dimers and localize to the plasma inner leaflet by non-specific electrostatic interactions. M proteins drive local outward curvature and play a pivotal role in viral assembly and budding. Inhibiting virion release from infected cells via interference with this protein host-cell interactions such as actin could impede viral dissemination. For example, in the case of Measles virus (MeV), inhibiting actin filament elongation has been shown to hinder viral budding [25]. Moreover, certain paramyxoviruses directly interact with purified actin. For instance, both Sendai virus (SeV) and Newcastle disease virus (NDV) M proteins have demonstrated direct interactions with actin [15]. In the context of SeV, a potential actin-binding motif was identified in the C-terminal region of the Matrix protein [27]. Additionally, a proteomic-based interaction study has identified several important actin regulators, particularly those involved in cytoskeleton remodeling, such as cofilin and the ARP2/3 complexes, as binding partners for NiV-M protein [22]. Hence, our research question is does the actin cytoskeleton regulate the formation of NiV-M arrays on a nanoscale. To answer our research question, we are using single-molecule localization microscopy to quantify the organization of NiV-M assembly sites on a nanoscale at the plasma membrane. We hypothesize that NiV-M-actin association facilitates the formation of large nanoscale NiV-M array and prepares them for budding.

## 2.2 Specific aims

To test our hypothesis, this project has the two following objectives:

1. To determine the interaction between actin and NiV-M, and its role in virus budding.
2. To determine whether NiV-M nano-organization at the plasma membrane can be affected by actin cytoskeleton using SMLM.

To achieve the objectives, we employed classic biochemistry and molecular biology approaches to identify potential NiV-M actin-binding motifs and to probe the role of actin in NiV VLP budding. For the second objective, we utilized Single-Molecule Localization Microscopy (SMLM) imaging to investigate the nano-organization of NiV-M and how it is stabilized by actin cytoskeleton.

### **3. Methodology**

#### **3.1 Cell culture**

HEK293T (ATCC CRL-3216) cells and PK13 (pig kidney fibroblast, American Type Culture Collection; ATCC, CRL6489) were cultured using Dulbecco's Modified Eagle's Medium (DMEM) from Sigma-Aldrich (D6429) with 10% Fetal Bovine Serum (FBS) from Thermo Fisher Scientific (12483020). Cells were screened for mycoplasma using a PCR-based mycoplasma detection kit (ABM, G238). Cells were grown at 37°C and 5% CO<sub>2</sub> Incubator.

#### **3.2 Expression plasmids**

A NiV-M-GFP expression plasmid was a kind gift from Dr. Keng Chou at the University of British Columbia. [30]. A 3x FLAG tagged NiV-M was construct as follows: NiV-M (GenBank: EU480491.1) was cloned into a pCMV-3Tag-1 vector (Stratagene) to generate 3XFLAG-M and a GFP sequence was fused in-frame to the N-terminus of NiV-M by Wang YE et al. To remove the GFP we mutated NotI to HindIII using the Q5 site-directed mutagenesis kit (E0552S). The primers were designed using the NEBaseChanger (<https://nebasechanger.neb.com/>) suggested by the kit; forward primer: 5'ccgcGAGCCCGACATCAAGAGC3' and reverse primer: 5'ccgcGATATCGAATTCCTGCAGC3'. The PCR protocol was followed according to the instructions of the kit. After the mutation, the GFP was flanked on each side with HindIII.

The enzyme HindIII was used to cut out the GFP (ThermoFisher 854671). The digestion product was run on an agarose gel and plasmid without the GFP was extracted from the gel using the QIAquick gel extraction kit (28704). The product was ligated using T4 DNA ligation (TM0202T). The plasmids were always transformed into stellar competent bacterial cells (Takara 636763) and kanamycin plates were used to select colonies. The plasmid was purified with the

miniprep kit (Biobasic, BS414-250 preps) and was sent for sequencing via Nanuq genome Quebec (<https://genomequebec.com/en/nanuq/> ).

The NiV-M mutants, I349A, K351A, P328A, and P332A, were generated by using the Q5 site-directed mutagenesis kit (E0552S) in both the 3xFLAG- and GFP-tagged versions. The primers were designed using the NEBaseChanger (<https://nebasechanger.neb.com/> ) suggested by the kit; forward primer: for I349A mutant 5' CACCGGCCGGgccCTGAAGGGCT3' and reverse primer: 5' TTGTCGATGAACACGTCGTCG3', forward primer for K351A mutant 5' CCGGATCCTGgccGGCTGATGAC3' and reverse primer: 5' CCGGTGTTGTCGATGAAC3', forward primer for mutant P328A and P332A 5' atcgccCGGGAGTTCATGATCTACGACGACGTG3' and reverse primer: 5' gctggcCTGCAGCACGGCGGCCAC3'. The instruction given by the Q5 kit were meticulously followed. The PCR product was then transformed into stellar competent cells and ampicillin plates were used for the GFP-tagged NiV-M mutants (in pcDNA 3.1+ vector) and Kanamycin plates for the 3xFLAG tagged mutants (in pCMV vector). The plasmids were purified using miniprep kit (Biobasic, BS414-250 preps) and sent for sequencing to Nanuq Genome Quebec (<https://genomequebec.com/en/nanuq/>). We noticed that one of the plasmids we sent had an extra deletion in the PxxP motif, the prolines were mutated to alanine's, but the Serine was deleted. We decided to use this mutant P328A( $\Delta$ S)P332A as well.

### **3.3 PCR**

The PCR protocol was derived from the Q5-site directed mutagenesis kit. Primers were designed using NEBaseChanger, with their sequences detailed in the 'Expression Plasmids' section of the Materials and Methods. PCR reagents were assembled as follows: 12.5  $\mu$ l of Q5 hot start high-fidelity 2x Master Mix, 1.25  $\mu$ l of 10  $\mu$ M forward primer, 1.25  $\mu$ l of 10  $\mu$ M reverse primer, 1  $\mu$ l

of template DNA, and 9  $\mu$ l of nuclease-free water, making a total volume of 25  $\mu$ l. For the PCR, the following thermal cycling settings were employed on a PCR Biometra machine: initial denaturation at 98°C for 30 seconds, followed by 25 cycles of denaturation at 98°C for 10 seconds, annealing at 66°C for 30 seconds, and extension at 72°C for 3 minutes. A final extension was performed at 72°C for 2 minutes, followed by a hold at 4°C. Subsequently, the PCR product was analyzed on a 1% agarose gel with a 1:10,000 dilution of SYBR Safe in TAE buffer, along with a DNA ladder (R1161). This step aimed to confirm that the fragment size aligned with the entire plasmid size even after mutagenesis.

### **3.4 Cell seeding & Transfection of plasmids.**

PK13 were seeded on coverslips (18 mm, 1.5 H, Marienfeld) pre-coated with 2.5  $\mu$ g fibronectin (Sigma-Aldrich) and filtered tracking beads at a concentration of 1:300 1.5  $\mu$ l per coverslips (Thermofisher F8799) in a 12-well plate. On the day following seeding, cells were transfected using the Lipofectamine reagent (Thermofisher L3000015). For each coverslip, 1  $\mu$ g of plasmid was transfected.

### **3.5 Immunofluorescence for SMLM**

24 hours post-transfection PK13 cells were fixed with 4% paraformaldehyde (PFA) (Fisher 50980487) and 0.2% glutaraldehyde (Sigma-Aldrich G5882) for 90 min. Cells were permeabilized with 0.1% TritonX-100 for 5 min (Sigma-Aldrich T8787) for detection of NiV-M-GFP. Coverslips were incubated 30 min with signal enhancer Image-IT-Fx (Life Technologies) and then left in blocking solution for 1 hour at room temperature (Bloackaid Thermofisher B10710). For single-color imaging of NiV-M GFP, the following antibodies were employed: the primary antibody Rabbit anti-GFP monoclonal antibody (Invitrogen, G10362) at a 1:600 dilution,

and the secondary antibody, donkey anti-rabbit 647 (A31573), at a 1:400 dilution. Both antibodies were diluted in the blocking solution. The primary antibody was incubated overnight at 4°C, while the secondary antibody was incubated for one hour at room temperature. After each antibody incubation, the samples were washed 5x using phosphate-buffered saline (PBS). Finally, cells were fixed using 4% PFA for 10 min at room temperature [30].

### **3.6 LatA and DMSO treatment**

24 hours post-transfection PK13 cells were treated with 1µM Latrunculin A (LatA) (428021) or 1µM dimethyl sulfoxide (DMSO) (Sigma-Aldrich, D8418) as control [36]. The LatA and DMSO were diluted into 1 mL pre-warmed DMEM and added for 5 min to the cells. The medium was then aspirated, and cells were washed twice with pre-warmed PBS before being fixed with 4% paraformaldehyde (PFA) (Fisher 50980487) and 0.2% glutaraldehyde (Sigma-Aldrich G5882) for 90 min. The same protocol explained in “3.5 Immunofluorescence for SMLM” was followed for imaging.

### **3.7 SMLM set-up**

The home-built microscope was constructed by Dr. Liu. It contains four lasers used for excitation but only 3 of them were used during experiments: the 639 nm laser (Genesis MX639, Coherent) was used to excite Alexa Fluor 647, the 488 nm laser (DHOM-100B, Fine Mechanics) for exciting GFP and a 405 nm laser (LRD 0405, Laserglow Technologies) for re-activating Alexa Fluor 647. These lasers are coupled to an inverted microscope with a TIRF oil-immersion objective lens (60×; numerical aperture 1.49; Nikon). Tracking beads (Thermofisher F8799) are seeded on coverslips to correct for the sample drift during acquisition of images. Therefore, allowing the position of the sample to lock during image acquisition [30].

### 3.8 SMLM image acquisition and reconstruction

At the beginning of an SMLM experiment, all fluorophores are in the ON state, allowing us to distinguish cell shapes and capture a widefield image. Then, a majority of the fluorophores are turned OFF by intense excitation of around  $10\text{--}30\text{ kW cm}^{-2}$  at the appropriate wavelength. This generates single-molecule fluorescence. The OFF state lasts for several seconds, followed by reversion to the ON state upon interacting with residual oxygen. The ON state's duration for these fluorophores typically ranges from 5 to 20 ms, with thiol and oxygen scavenger concentrations affecting the blinking efficiency [31].

Immunolabeling is employed to label the protein of interest. This standard method involves an antibody binding specifically to the target protein, while a secondary antibody coupled with a photoswitchable dye complements the binding [31].

For single-color imaging, coverslips were immersed in an oxygen-savaging buffer containing 50 nM mercaptoethylamine (MEA). During imaging, cells were selected as positive based on their fluorescent intensities, which needed to be at least three times higher than the negative control. NiV-M expression was assessed using the 488 nm laser (DHOM-100B, Fine Mechanics) to excite GFP. In instances where a cell was infected with NiV-M, clusters could be observed at the plasma membrane. After identifying positive cells, a laser power density of  $1\text{ kW cm}^{-2}$  was utilized for the 639 nm laser to activate the Alexa Fluor 647. The camera acquired 40,000 frames for a single SMLM image. MATLAB (MathWorks) was the software employed for image reconstruction [30, 37].

### **3.9 Western blot for VLP budding assay**

Equal amount of VLP and cell lysate were prepared with 5x loading dye and final concentration of 5%  $\beta$ -mercaptoethanol (BME) added, boiled at 100°C, and were then loaded on 12.5 % SDS-PAGE. SDS-PAGE was run at 85V until the bands reached the separation gel, then it was run at 135V. The SDS-PAGE gel was then transferred to an activated polyvinylidene difluoride (PVDF) membrane (Sigma-Aldrich, IPVH00005) and ran at 400A for 90 minutes. The PVDF was then blotted using 1% Bovine Serum Albumin (BSA) Blocking Buffer in PBS for 1h30 at room temperature. For the pCMV-3Tag-1 vector (Stratagene), anti-flag antibodies were employed: Mouse anti-flag at 1:5000 dilution (Sigma F1804), and Goat anti-mouse HRP at 1:5000 dilution (Biorad, 1705047). For the GFP-tagged NiV-M constructs, a primary antibody of rabbit anti-GFP at 1:100 dilution (Invitrogen, G10362) was used, followed by a secondary antibody of Goat anti-rabbit HRP at 1:5000 dilution. As the loading control, a primary antibody of mouse anti-GAPDH at 1:5000 dilution (Millipore, CB1001) was employed, with a secondary antibody of donkey anti-mouse at 1:5000 dilution. The primary antibody was incubated overnight at 4°C and then the next day was washed off 5x with 0.05% PBST. The secondary antibody is incubated for 1 hour at room temperature and then washed off 5x with 0.05% PBST. The membranes were then coated with Biorad western ECL substrate (Bio-rad, 1705060) for imaging using the Chemic Doc MP Imaging System BioRad.

### **3.10 VLP production and Cell lysate preparation**

HEK293T (ATCC CRL-3216) cells were seeded 1:3 into 10 cm or 15 cm dish and transfected using polyethyleneimine (PEI) transfection reagent (02371/500, Polysciences). For the GFP-tagged NiV-M constructs, 60 ug of plasmid was transfected into a 15 cm dish. For the 3x FLAG-tagged NiV-M constructs, 30 ug of plasmid was transfected in 15 cm dish. The transfection mix was added to the dish containing the cells and incubated at 37C 5% CO<sub>2</sub> for 7-8hrs. The medium (DMEM with 10% FBS) was then replaced by fresh growth medium pre-warmed at 37°C. Cells were incubated for 48 hours in the cell incubator. The cell supernatant was collected into a 50 ml tube and spun 300 rcf for 5 min. The supernatant was filtered using 0.45 uM filters. VLPs were then collected on a 20% sucrose in NTE buffer cushion by ultracentrifugation at 100 000g. The supernatant was gently aspirated and VLPs were resuspended in 5% sucrose-NTE buffer. VLPs were aliquot and stored at -80C. As for the cell lysate, lysis buffer was made of radioimmunoprecipitation assay (RIPA buffer Sigma-Alderich, 20-188) and EDTA-free Protease Inhibitor Cocktail (Sigma-Alderich, 11836170001). The dishes were incubated on ice for 30 min while shaking and then kept at -80C. Cell lysates were then spun at 16 000 rcf for 20 min at 4C. The supernatant was then stored at -80C or short-term storage -20C until further Western Blot analysis [30].

### **3.11 Statistical analysis**

To obtain statistical data the p values were calculated by GraphPad Prism 7 software by using the T test (non-parametric) with Welch's correction. P values are non-signifiant (ns)  $p > 0.05$ , \* $P \leq 0.05$ , \*\*  $P \leq 0.01$ , \*\*\*  $P \leq 0.001$ , \*\*\*\*  $P \leq 0.0001$

### **3.12 VLP budding assay.**

VLP collected from HEK293T (ATCC CRL-3216) cells transfected with the GFP-tagged NiV-M constructs and 3x FLAG-tagged NiV-M constructs were analyzed using Western Blot. The intensity of the bands was quantified by the densitometry with Image J. To calculate the budding index, expression of NiV-M constructs in the cell lysate was normalized to that of the Glyceraldehyde 3-phosphate dehydrogenase (GAPDH) control, and the normalized expression of NiV-M mutants was further normalized to that of the WT. A similar method was used to normalize the expression of the NiV-M constructs in VLPs to that of the wt. The budding index was then calculated by calculating the ratio VLP divided by the ratio of the cell lysate. The budding index values were then input in prism to calculate P values. [38].

### **3.13 Immunofluorescence for confocal microscopy.**

12 mm coverslips were coated with 1.25  $\mu$ g of fibronectin. To visualize the NiV-M VLPs and their actin incorporation, the VLP preparations for the GFP tagged wt NiV-M, I349A, and K351A mutants were utilized. The VLP production protocol from section 3.10 of the Materials and Methods was followed. Each sample was diluted 1:3 in Infection buffer (PBS + 0.1% FBS) to achieve a total volume of 80  $\mu$ l per coverslip. For instance, for NiV-M GFP WT, 20  $\mu$ l of the VLP preparation from 2023-04-24 was mixed with 60  $\mu$ l of infection buffer. This 80  $\mu$ l mixture was then transferred to the coverslip and allowed to incubate at 4°C overnight. The same procedure was repeated for the I349A and K351A mutants. To observe DMSO-treated cells versus LatA-treated cells using confocal microscopy, we prepared 12 mm coverslips coated with 1.25  $\mu$ g of fibronectin. PK13 cells were then seeded in a 24-well plate. The following day, the cells were transfected with NiV-M GFP WT. After 24 hours post-transfection, PK13 cells were treated with either 1  $\mu$ M LatA (428021) or 1  $\mu$ M dimethyl sulfoxide (DMSO) as a control [27]. Both LatA and

DMSO were diluted into 1 mL of pre-warmed DMEM and added to the cells for a 5-minute incubation, following the same protocol as outlined in Section 3.6 of the Materials and Methods. The fixation and staining protocol for confocal microscopy remained consistent, whether for the VLP samples or the LatA and DMSO-treated cells. In the case of the LatA and DMSO samples, fixation occurred immediately after drug treatment, while for VLP preparation, it was incubated overnight before fixation. The samples underwent two brief washes with PBS before fixation with 100 µl of 4% PFA for 30 minutes at room temperature. After fixation, the samples were transferred to a 24-well plate and subjected to three 5-minute washes. Permeabilization was performed using 0.1% Triton X-100 for 5 minutes, followed by blocking in a solution of BlockAid (Thermo Fisher) for 1 hour at room temperature. Subsequently, the primary antibody, mouse anti-beta actin at 1:100, was incubated for 1 hour at room temperature, and then washed five times with PBS. The secondary antibody, donkey anti-mouse 647 at 1:400, underwent the same incubation period and washing steps. The coverslips were mounted on microscope slides (VWR, 16004-369) using Prolong™ Diamond Antifade Mountant (Thermo Scientific P36961) and left overnight at room temperature. To seal the coverslips, nail polish was applied. Finally, imaging was performed using the LSM710 confocal microscope.

### 3.14 Co-Immunoprecipitation

The 3x FLAG-tagged NiV-M constructs (WT, I349A, and K351A) were transfected into HEK293T (ATCC CRL-3216) cells. As a negative control, an empty pcDNA3.1 vector was used. Approximately 24 hours post-transfection, cells were washed with PBS and lysed in 400  $\mu$ L of RIPA buffer (Millipore, MA) supplemented with complete protease inhibitor (cOmplete mini; Roche, IN). The cells were lysed for 30 minutes on ice, and cellular debris was removed by centrifugation. Half of the cell lysate was used for immunoprecipitation, employing the  $\mu$ MACS™ and MultiMACS™ DYKDDDDK Isolation Kits (Miltenyi Biotec). The lysates were incubated with 20  $\mu$ L of Anti-Flag MicroBeads on ice for 30 minutes. The labeled mixture was added to the column, followed by a wash, following the provided instructions. Subsequently, 50  $\mu$ L of preheated Elution Buffer (containing 50 mM DTT) at 95°C was added to the column, and the eluate was collected. Both the purified eluate and the original lysed cell lysate were separated by 10% PAGE and transferred onto a polyvinylidene difluoride (PVDF) membrane. Detection of 3x FLAG-tagged NiV-M and  $\beta$ -actin was performed using mouse anti-Flag antibody (1:1000, Sigma) and mouse anti- $\beta$ -actin antibody (1:2000, Sigma), respectively. Secondary antibodies (Goat anti-mouse HRP, BIO-RAD) were applied at a 1:2000 dilution. Western blots were imaged using the ChemiDoc XRS system (Bio-Rad, CA), and protein bands were quantified using Quantity One analysis software (Bio-Rad, CA).

### **3.15 Nipah matrix structure**

The NiV-M structure was obtained from the Protein Data Bank (PDB) using the website rcsb.org. The NiV-M PDB code is 7SKT. Residues crucial for dimerization and membrane association were identified by Norris et al. Specifically, residues 118, 128, 305, and 339, critical for dimerization, are highlighted in yellow, while residues 64, 95, 143, 152, 155, 304, and 191, essential for membrane association, are marked in blue. The KLKK-like motif spans amino acids 348 to 352, depicted in orange, and the PxxP motif from 328 to 332 is shown in green [19].

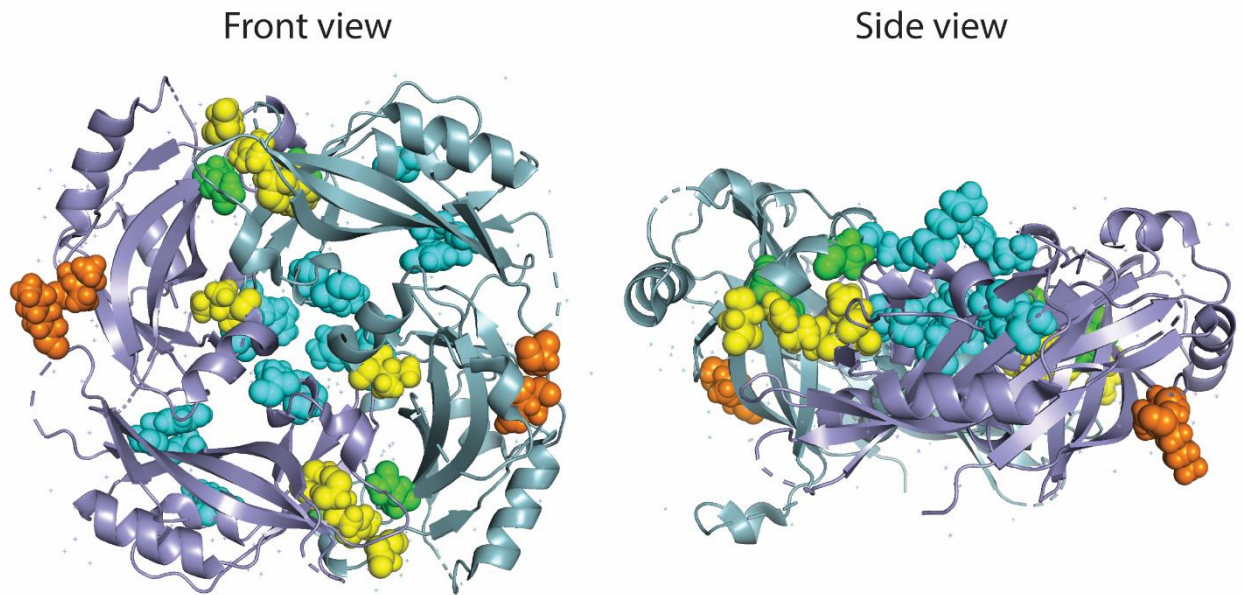
## **4.Results:**

### **4.1 NiV-M possesses a PxxP and KLKK-like motifs shared among some paramyxoviruses and actin-binding proteins.**

Previous research suggests that some paramyxoviruses such as both Sendai virus (SeV) and Newcastle disease virus (NDV) M proteins might directly interact with actin cytoskeleton [15]. For SeV, a putative actin-binding motif was identified at the C-terminal of the matrix protein and resembled a KLKK like motif essential for actin-binding [27]. To explore this further, we employed the ClustalX2 program to align the protein sequences of NiV-M, Human parainfluenza virus 1 (hPIV-1-M), SeV-M, and two actin-binding proteins (WASP and WASF2). From this alignment, two regions exhibited homology across all proteins: the proline residues at positions 328 and 332 forming a PxxP motif were conserved among viral and actin-binding proteins (Fig. 10 A). The PxxP motif is commonly found in actin-binding proteins like WASP, featuring proline-rich regions that facilitate interactions with proteins containing Src-homology-3 (SH3) domains and profilin. Moreover, they also play a role in enhancing the activation of Arp2/3 [39]. Furthermore, NiV-M displayed the same putative actin-binding motif "KLKK" spanning amino acids 347 to 341 (Fig 10 A). Within the KLKK motif, we identified homologous residues: isoleucine 349 (I349) was conserved across viral and actin-binding proteins, while lysine (K351) was exclusively conserved among viral proteins (Fig. 10 B). In the PxxP motif, proline 328 and proline 332 were conserved across viral and actin-binding proteins, except for WASF2. Isoleucine 331 was conserved only among viral proteins (Fig. 10B)



## NiV-M dimer



Orange: KLKK-like motif (putative actin-interaction)  
Green: PxxP motif  
Cyan: Membrane association  
Yellow: Dimerization

**Figure 11.** The PxxP and KLKK-like motifs do not hinder membrane association or dimerization. Key residues for membrane association (cyan) and dimerization (yellow) are distinct from the KLKK-like motif (orange) and PxxP motif (green). On the left, NiV-M dimer crystal structure front view and on the right; side view. NiV-M structure was modelled using the PyMOL software (<https://pymol.org/2/>)<sup>17</sup>.

## 4.2 Mutagenesis studies of PxxP and KLKK-like motifs.

Next, we generated two distinct mutants for each motif - PxxP and KLKK. This was accomplished utilizing the Q5 site-directed mutagenesis kit, wherein crucial amino acids were substituted with alanine as described in *Materials and Methods*. In the case of the KLKK motif, the conserved isoleucine 349 (I349) - found in both viral and actin-binding proteins - was mutated in the first variant, while the second variant involved the mutation of lysine (K351), another conserved amino acid among viral proteins (Fig 12. A). In the PxxP motif, the two proline residues at positions 328 and 332 were substituted with alanine. These residues were conserved among viral and actin-binding proteins. The second mutant included an additional deletion of the isoleucine residue, which was only conserved among viral proteins (Fig. 12B).

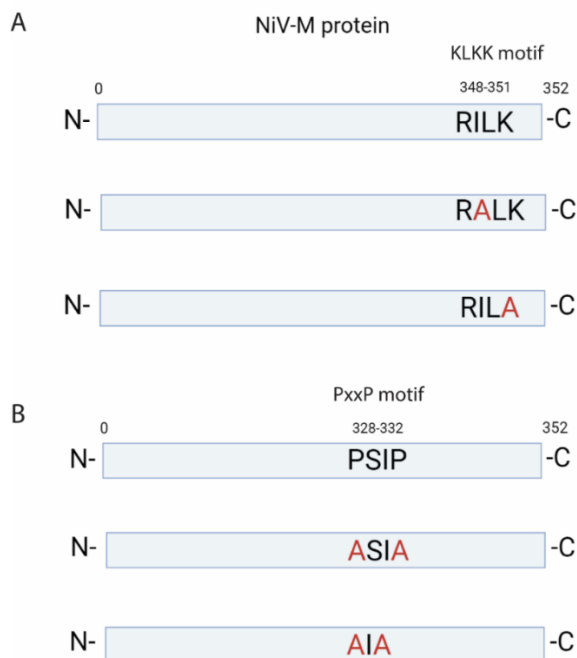


**Figure 12. Mutagenesis of PxxP and KLKK-like motif.** Regarding the KLKK-like motif, two mutants, I349A and K351A, were generated from the WT NiV-M. For the PxxP motif, two mutants, P328AP332A and P328A( $\Delta$ )P332A, were created.

To evaluate whether the mutation impacted cellular expression or VLP production, western blot analyses were conducted. As previously mentioned, NiV-M can form viral-like particles (VLPs) on its own. Thus, in transfected cells, NiV-M VLPs will be released into the culture supernatant [38]. NiV-M WT, I349A, K351A, P328AP332A, and P328A( $\Delta$ S)P332A mutants were fused with a GFP and a 3x FLAG tag and cloned into the pcDNA3.1+ and pCMV-3Tag-1 vectors, respectively. 3x FLAG tagged NiV-M WT and mutants were transfected into 293T cells. Cell lysates of all mutants were comparable to WT, except for the P328A( $\Delta$ S)P332A mutant which exhibited slightly lower NiV-M cellular expression (Fig 13 A). The empty vector pcDNA3.1+ was used as a negative control, yielding a small band likely from overflow from the other wells (Fig 13 A). To ensure the control was effective, we repeated the western blot using cells that were transfected with the empty vector pcDNA3.1+ and the 3x FLAG-tagged NiV-M WT. No bands were observed in the cell lysate or VLP detection (Figure 13 B). GAPDH served as the loading control, displaying consistent bands across all samples (Fig. 13). No bands of the PxxP mutants P328AP332A and P328A( $\Delta$ S)P332A were detected in VLP. Among the KLKK mutants, we observed bands in VLP, in contrast to the PxxP mutants (Fig. 13A). Due to time constraints, we opted to focus on the KLKK mutants for my master's project. This motif had previously been identified as a potential actin-binding motif [17]. The I349A mutant exhibited significantly lower budding compared to WT, while the K351 mutant displayed slightly lower budding without statistical significance (Fig. 13C). For imaging, we used GFP-tagged NiV-M. We subsequently repeated the Western Blot using the GFP-tagged version. We analyzed VLP production of both 3x FLAG- and GFP-tagged NiV-M constructs to rule out the potential effect of the epitope tags on the assembly and budding ability of NiV-M. The western blot for the GFP-

tagged WT, I349A, and K351A NiV-M mutants revealed consistent expression patterns in cell lysates (Fig. 13D). Agreeing with the findings for the 3xFLAG-tagged NiV-M constructs, we observed reduced NiV VLP budding in the GFP-tagged mutants. This reduction was indicated by weaker bands compared to the wild-type (WT) (Fig. 13 D). Similar cell lysates were observed between I349A and WT, although K351 showed stronger bands in cell lysate. GAPDH served as the loading control, displaying consistent loading across all samples (Fig. 13D). The relative budding index of the GFP-tagged NiV-M mutants were significantly lower than that of the WT (Fig. 13E), similarly to the results from the 3xFLAG tagged NiV-M constructs (Fig 13C). This confirmed that the epitope tags on NiV-M constructs do not have a significant impact on its function (Fig. 13). These experiments inform that mutations in the KLKK motif decrease significantly the budding of NiV VLPs.

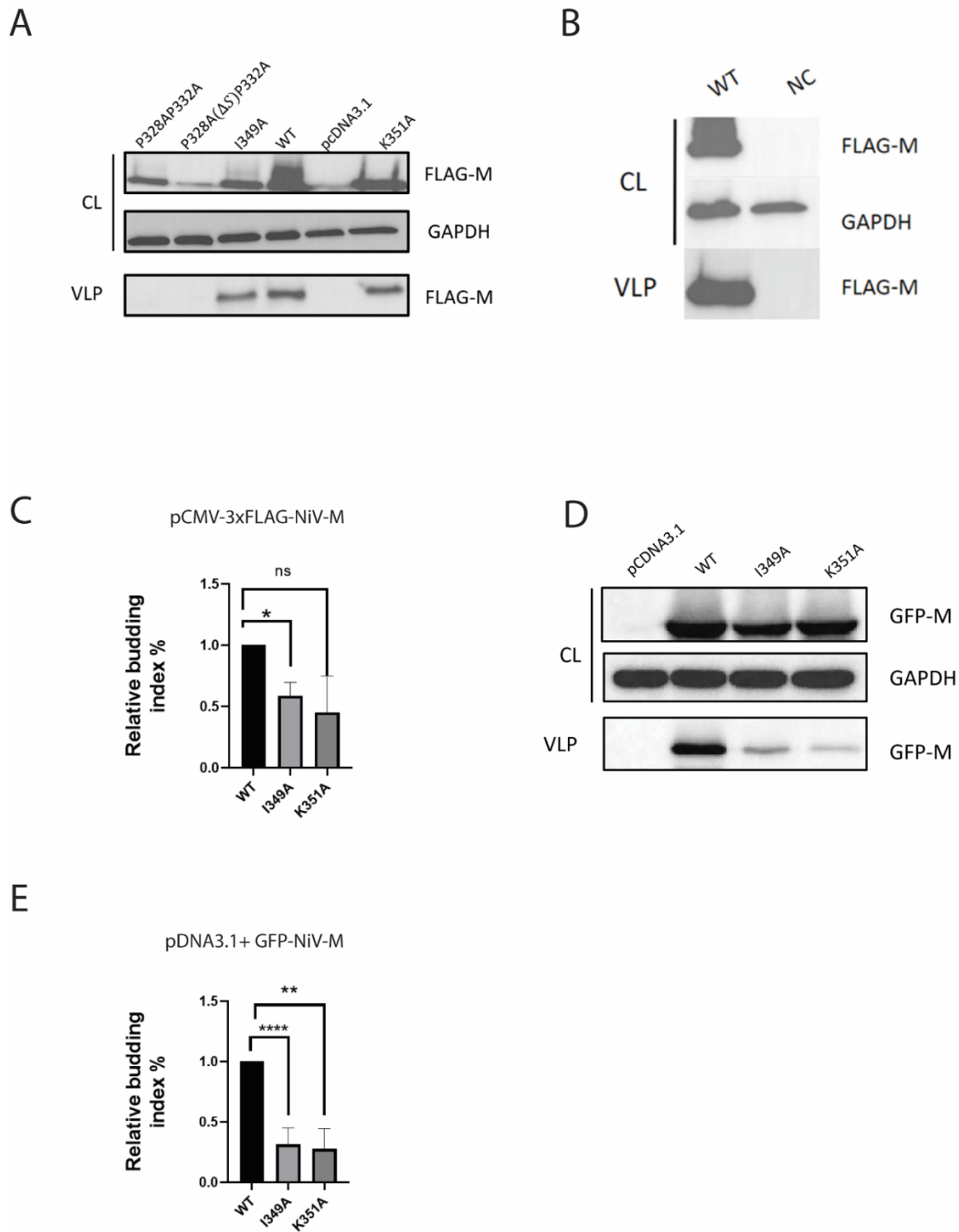


**Figure 13. Functionality of the mutants created by comparing cellular lysate and VLP expression.** (A) VLPs and cell lysate were harvested from 293T cells transfected with pCMV-3Tag-1 NiV-M-FLAG, KLKK mutants (I349A and K351A) and PxxP mutants (P328AP332A and

P328A( $\Delta$ S)P332A) and analyzed using Western Blot as described in Materials and Methods. VLPs and cell lysates were immunoblotted with an anti-FLAG antibody for NiV-M detection and anti-GAPDH for loading control. The empty pcDNA3+ vector was transfected as a negative control. (B) The Western blot was repeated, and VLPs and cell lysates from A, including pCMV-3Tag-1 NiV-M-FLAG and the empty pcDNA3+ vector, were used for loading. (C) The relative budding index was calculated by determining the ratio of VLP intensity to cell lysate intensity, normalized to WT, based on three independent repetitions of western blot analysis. (D) Same experiments in A were repeated with GFP-tagged WT NiV-M, I349A, and K351A. VLPs and cell lysates were immunoblotted with an anti-GFP antibody for NiV-M detection and anti-GAPDH for loading control. (E) The relative budding index was calculated as in B. based on three independent repetitions of western blot analysis. Prism software was used to plot B. & D and p value was calculated using student t test with Welch's correction. P values are indicated as non-significant ns  $p > 0.05$ , \* $P \leq 0.05$ , \*\*  $P \leq 0.01$ , \*\*\*  $P \leq 0.001$ , \*\*\*\*  $P \leq 0.0001$ .

### **4.3 A putative actin-binding domain at NiV-M is key for virus budding and actin incorporation in VLPs.**

Next, we investigated the potential interaction between NiV-M and the actin cytoskeleton.

Previous research has demonstrated such interactions in certain paramyxoviruses like Sendai and MeV [15]. We hypothesized that mutations within the KLKK motif reduced NiV-M-actin association. To address this, we collected supernatant and cell lysates from 293T cells transfected with pCMV-3xFLAG-tagged NiV-M WT, I349A, K351A, and a negative control (empty vector). As anticipated, all NiV-M constructs, whether WT or mutated, showed increased levels of  $\beta$ -actin compared to the empty vector control in the supernatant (Fig. 14A). The  $\beta$ -actin detected in the supernatant of the negative control may result from the release of actin via an NiV-M independent manner, such as the extracellular vesicles. These findings strongly indicate that actin is likely incorporated into the VLPs. Thereafter, we used confocal microscopy to examine the VLPs (Fig. 14B). By using VLPs produced from 293T cells expressing GFP tagged NiV-M constructs, we were able to identify the VLPs by the GFP fluorescence while an anti- $\beta$ -actin antibody was used to label actin. We observed less colocalization between actin and NiV-M constructs in the I349A and K351A mutants compared to that of the WT NiV-M. By utilizing the Imaris software, we determined the percentage of actin-containing VLPs for VLPs produced by cells expressing both the WT and mutant NiV-M (Fig. 14C). As expected, mutations in the putative actin-binding motif led to a significant reduction in the percentage of actin-containing VLPs when compared to the WT (Fig. 14C). This suggests that the KLKK motif in NiV-M likely interacts with actin, as its mutation resulted in decreased actin incorporation into the VLPs. We then conducted co-immunoprecipitation to examine the protein expression levels of cellular NiV-M and  $\beta$ -actin. As expected, the results of these experiments indicated a clear interaction between

NiV-M and  $\beta$ -actin in WT cells. The K351A exhibited a weaker interaction than WT, although to a lesser extent than the I349A mutant (Fig. 14D). Nevertheless, actin association was not entirely impaired, as evident from the immunoblot data (Fig. 14).

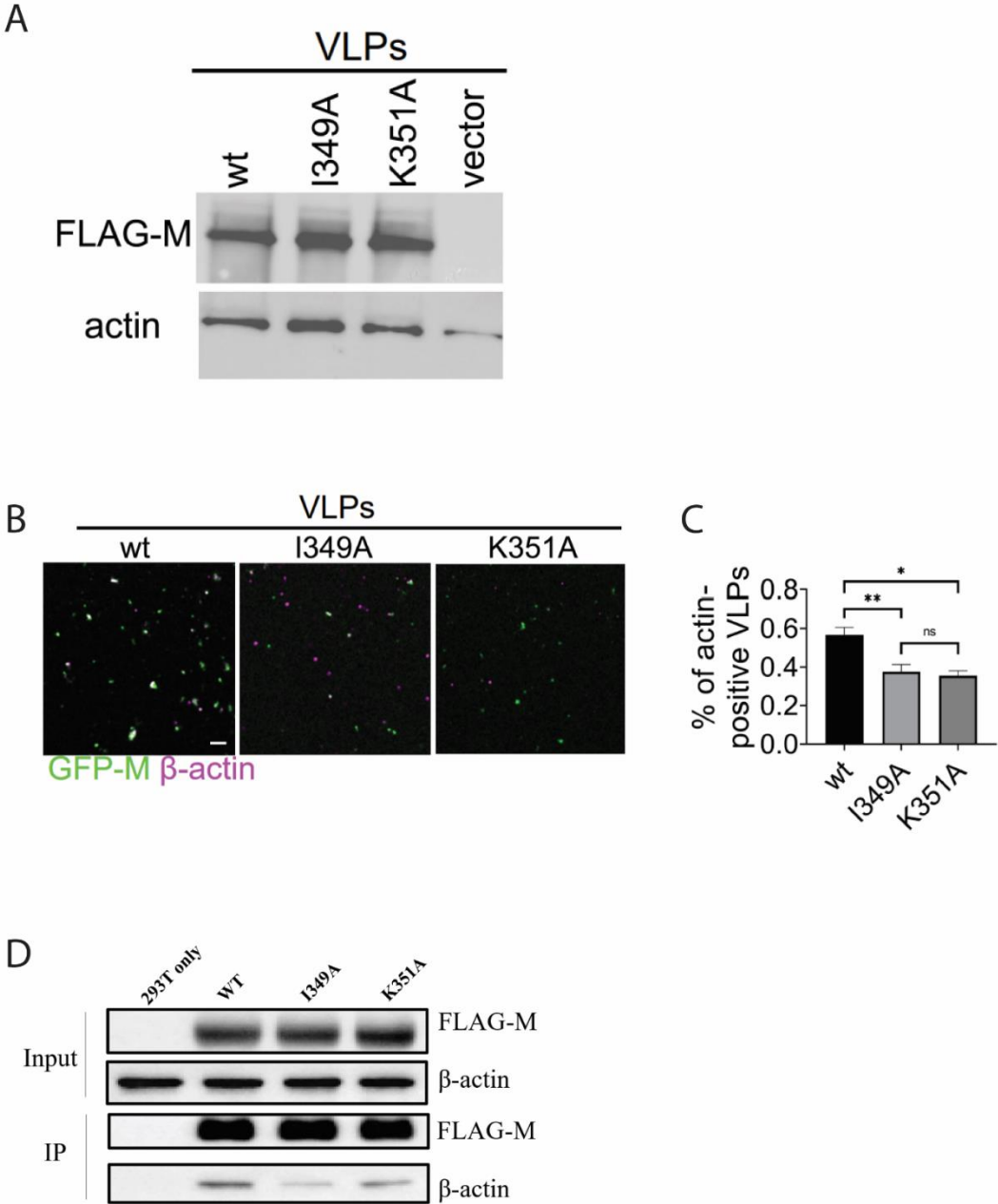


**Figure 14. Actin incorporation in NiV-M VLPs.** (A) VLPs were collected from 293T cells transfected with 3x FLAG-tagged NiV-M, I349A and K351 constructs and analyzed using

Western Blot. A mouse Anti-Flag antibody was used to detect NiV-M, and actin was detected using a mouse anti-beta actin antibody. Representative immunoblot result shown from over 3 independent experiments. (B) VLPs produced by 293T cells transfected by GFP-tagged wt NiV-M, I349A, and K351A were imaged using a laser scanning confocal microscope. VLPs (green) were detected through GFP fused with the NiV-M constructs and  $\beta$ -actin was stained with a mouse anti- $\beta$ -actin primary antibody and a donkey anti-mouse secondary antibody conjugated with Alexa Fluor 647 (magenta). (C) The percentage of actin-positive VLPs was calculated as the ratio of the number of  $\beta$ -actin-containing VLPs (GFP+/  $\beta$ -actin+) over the total number of VLP (GFP+) by the Imaris software. (D) For the co-immunoprecipitation assay, we transfected 293T cells with 3x FLAG-tagged NiV-M constructs (WT, I349A, and K351A) along with an empty pcDNA3.1+ vector. We detected 3x FLAG-tagged NiV-M and  $\beta$ -actin using mouse anti-Flag and mouse anti- $\beta$ -actin antibodies, respectively. Subsequently, we applied secondary antibodies, specifically Goat anti-mouse HRP. The p-values were determined using an unpaired student t test with Welch's correction: ns  $p > 0.05$ , \* $P \leq 0.05$ , \*\*  $P \leq 0.01$ , \*\*\*  $P \leq 0.001$ , \*\*\*\*  $P \leq 0.0001$ .

#### **4.4 Mutations at the putative actin-binding domain in NiV-M alter the nanoscale organization of NiV-M.**

Next, we investigated if mutation at the putative actin-binding motif would alter the nanoscale organization of NiV-M. Firstly, we transfected PK13 cells with GFP-tagged NiV-M and prepared samples for SMLM imaging as described in the *Material and Methods*. PK13 cells were chosen due to their large, flat morphology, and imaging was focused on their dorsal membrane, as depicted in Figure 15A. As previously mentioned, NiV-M assembles at the plasma membrane. Therefore, to visualize NiV-M assembly sites, cells were permeabilized and stained with Alexa Fluor 647. The reconstructed images are a result of 40,000 images acquired using high laser power to precisely map the localization of fluorophores (Alexa 647) with a lateral resolution of approximately 10 nanometers. NiV-M WT and mutants reconstructed images are shown in figure 15 B where cell shape can be discerned, and M proteins can be found in clusters on the plasma membrane consistent with previous papers [30]. The reconstructed images presented for each sample depict representative cells selected from a pool of WT with 16 cells, I349 with 9 cells, and K351 with 14 cells. For cluster detection, we employed Density-Based Spatial Clustering of Applications with Noise (DBSCAN) algorithm [40]. DBSCAN identifies closely grouped localizations and detects outliers. Specifically, for a localization to be considered part of a cluster, it must satisfy two criteria for connectivity. Firstly, it needs to have another localization equal to or greater than the MinPts (minimum number of neighbors, set to 3) within a defined radius 'r' of 10 nanometers. If the neighboring localizations themselves have MinPts neighbors or more, the cluster expands. However, if a localization lacks more than MinPts neighbors and is not connected to another localization, it is categorized as non-clustered (isolated molecule), as shown in Figure 15 C. DBSCAN was chosen for this project due to its ability to identify clusters with

irregular shapes, unlike the Ripley's K program, which tends to detect circular clusters. In our case, a cluster consisted of 10 or more NiV-M localizations (Fig. 15C) [25]. In the reconstructed images, a yellow rectangle outlines a region of interest (ROI) chosen for DBSCAN analysis. Approximately 10-20 ROIs were selected per cell. Enlarged ROIs (Fig. 15D) and their respective cluster maps are represented for each sample (Fig. 15E). The results of the DBSCAN analysis are depicted as cluster maps, where unclustered NiV-M localizations are represented in gray, and clustered localizations are highlighted in red. The I349 and K351 mutants exhibit a higher number of unclustered NiV-M localizations compared to the predominantly clustered NiV-M localizations of the WT (Fig. 15E).

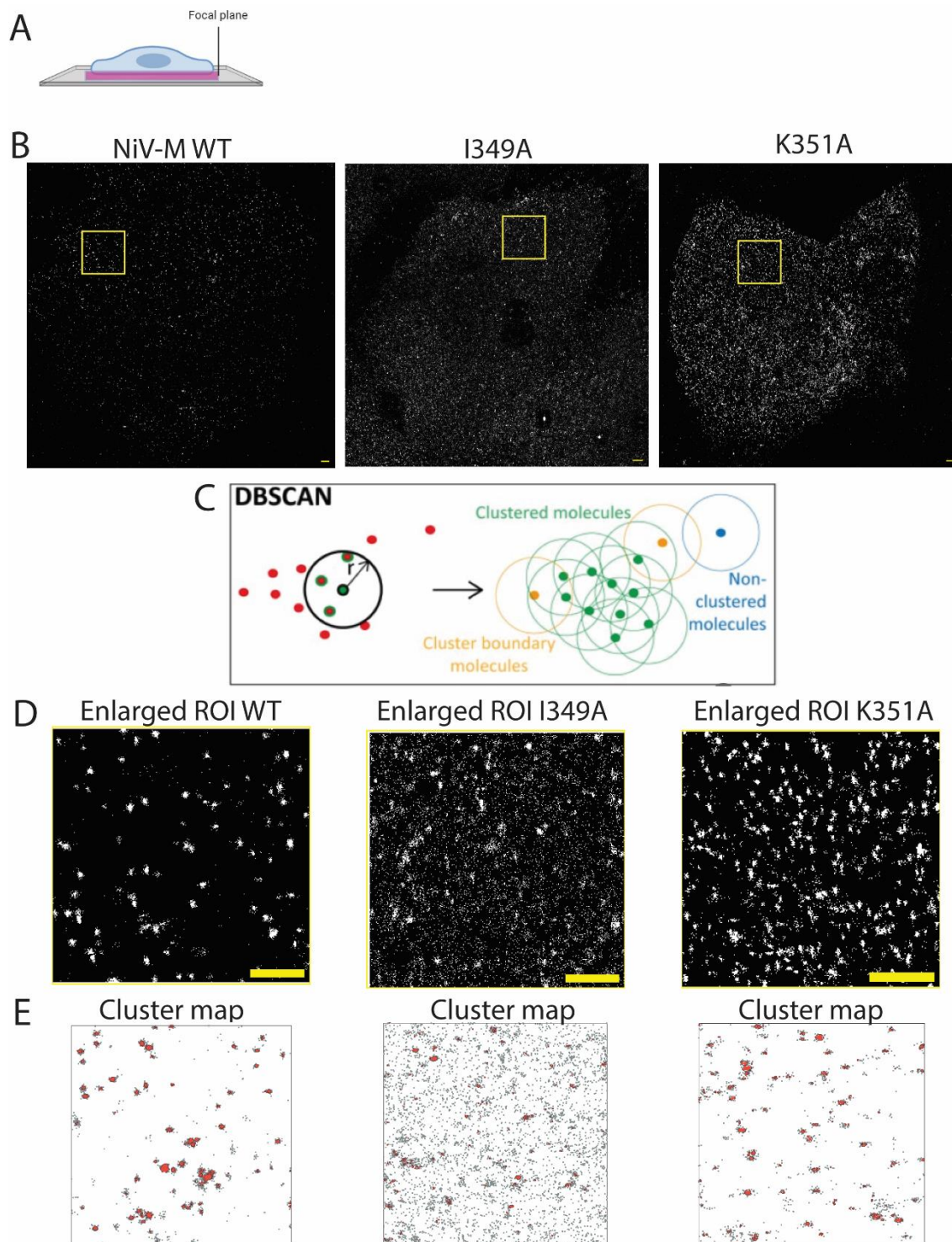


**Fig. 15.** The nano-organization NiV-M mutants within the KLKK-like motif show a different cluster pattern than WT. PK13 cells were chosen due to their large, flat morphology, and imaging was focused on their dorsal membrane (A). PK13 cells were transfected with the

GFP tagged NiV-M, I349A, and K351A. Immunostaining was performed 24 hours post-transfection. NiV-M was labeled using a rabbit anti-GFP primary antibody, followed by a donkey anti-rabbit secondary antibody conjugated with Alexa Fluor 647 (B). Super-resolution images were acquired using SMLM, and representative images for each sample were selected (B), with a cross-sectional view ( $\Delta z = 600$  nm) presented. Scale bar: 1  $\mu$ m. The DBSCAN figure is adapted from Pagoon, S. V., Nicovich, P. R., et al [25]. DBSCAN employs a propagative cluster detection approach for identifying clusters. When a localization meets the criteria within a given radius ( $r$ ), the connection is extended (green), and this process continues until the criteria are no longer met (yellow). Additionally, DBSCAN identifies isolated points or noise (blue) (C). The region of interest (ROI) is highlighted within a yellow box in images D. This boxed area is magnified in images, depicting the detailed distribution of NiV-M localizations. Scale bar: 1  $\mu$ m. Cluster analysis using DBSCAN was performed on the enlarged ROIs. The unclustered NiV-M localizations are shown in gray, while clustered NiV-M localizations are labeled in red on the cluster maps (E).

After identifying the clusters, we extracted specific statistical information, enabling us to discern differences in cluster distributions on the plasma membrane between the wild-type (WT) and mutant samples. Employing the density-based DBSCAN algorithm necessitates maintaining a consistent total average density (TAD) across all samples for meaningful comparison. In our statistical analysis, we defined regions of interest (ROIs) within cells, selecting approximately 10-20 ROIs per cell. TAD is calculated by dividing the total number of molecules within an ROI by its size, resulting in an overall density value. The I349A and K351A mutants displayed a non-significant variation in TAD when compared to the WT (Fig. 16A). Since the DBSCAN is a density-based algorithm, calculating the TAD is important because the difference in the cluster

distribution on the plasma membrane between WT and mutant samples is not caused by the density but by the nanoscale arrangement of these molecules. This means that the difference in clustering is not due to variable numbers of NiV-M localizations. We speculated that actin could potentially play a role in facilitating the creation of larger nanoscale NiV-M arrays, setting the stage for budding events. The I349A and K351A displayed different phenotypes compared to the WT similarly as observed with reconstructed SMLM images and cluster maps (*Figure 15,16*). The I349A mutant had the phenotype we anticipated (*Figure 16*). I349A mutation led to the emergence of smaller clusters (Fig. 16B). Specifically, the average cluster diameter (measured in nm) exhibited a significant reduction in the I349A mutant in comparison to the WT (Fig. 16B). Furthermore, these clusters contained a lower percentage of molecules per cluster for WT than for I349A (Fig. 16C). Relative density within clusters provides a measure of cluster density relative to the total average density within the ROI. To be more precise, the relative density is calculated by dividing the cluster density by the TAD. In Figure 16D, it was observed to be non-significant between WT and I349A as well as WT and K351A. Given that both the TAD and relative density showed non-significant values between WT and mutant samples, this suggests that cluster density remains similar between them. Consequently, molecules are packed in a similar manner within clusters. Despite I349A having fewer molecules in clusters and smaller clusters compared to WT, the cluster density remains non-significant when compared to WT (Fig. 16 B,C,D). Interestingly, circularity was lower for the I349A mutant compared to WT, but no significant change was observed for the K351A (Fig. 16E). Additionally, we employed Hopkins analysis to assess the cluster tendency of NiV-M localizations (Figure 16F). The Hopkins index spans from 0 (indicating a random distribution) to 1 (indicating extreme clustering) [21]. NiV-M demonstrated a higher cluster tendency compared to the I349A mutant, aligning with the observations from the cluster maps (Fig. 15). Within the cluster maps, NiV-M localizations

exhibited a greater presence within clusters than as non-clustered entities, in contrast to the I349A mutant where this trend was reversed (Fig. 15). In summary, the I349A mutant exhibited fewer molecules in clusters, smaller clusters, and lower cluster density compared to WT whereas K351 had no significance difference from the WT for all parameters (Fig. 16). These results show that mutation of I349 leads to dispersed distribution of NiV-M, suggesting a compromised assembly ability. These observations align with our initial hypothesis that the actin cytoskeleton could potentially facilitate the formation of large nanoscale NiV-M arrays. The K351A did not alter the nanoscale organization of NiV-M consistent with the similar phenotype seen in figure 15. In summary, the I349A mutant exhibited fewer molecules in clusters, smaller clusters, and lower cluster density compared to WT whereas K351 had no significance difference from the WT for all parameters (Fig. 16).

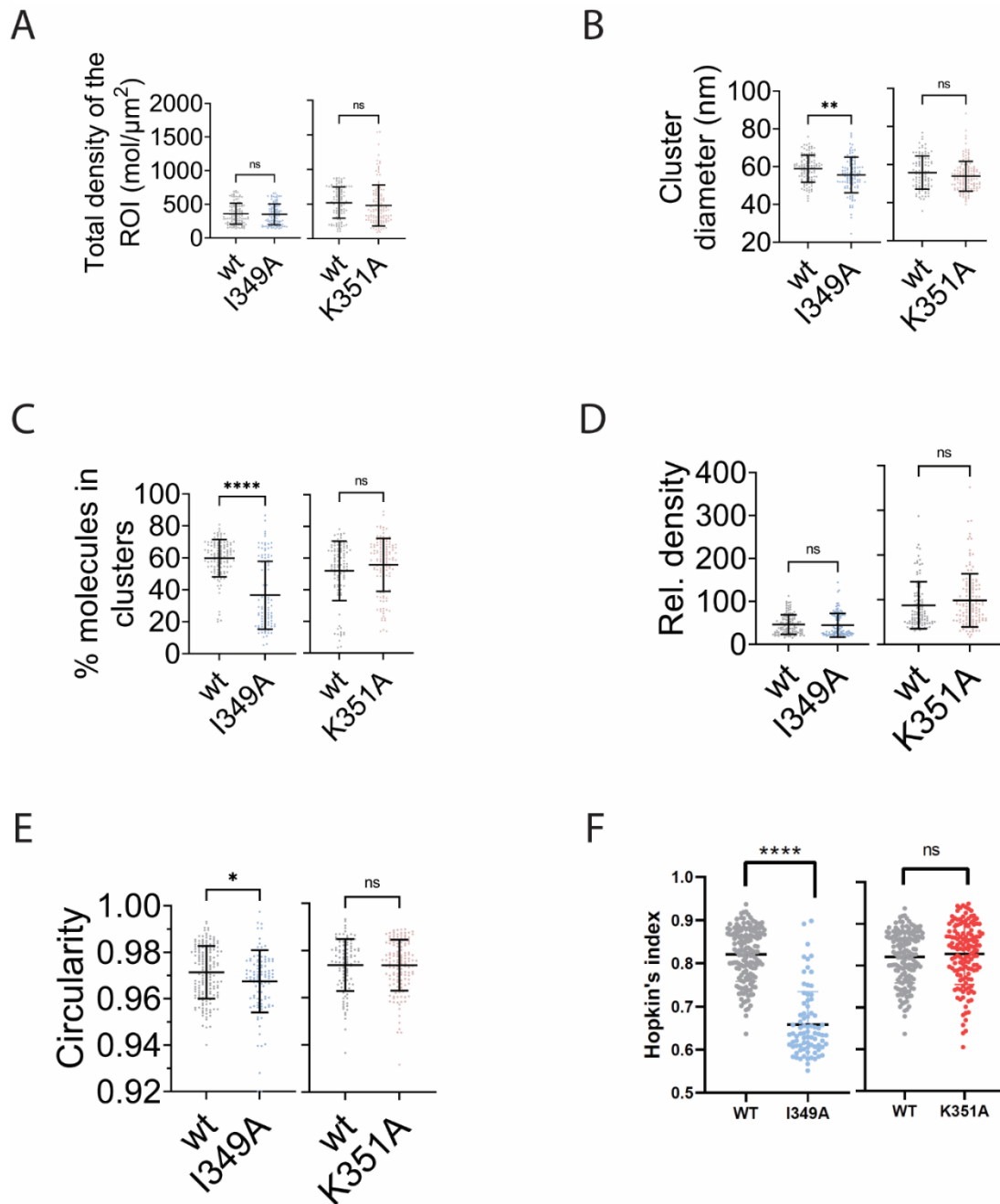


**Figure 16: The I349A mutation alters the nanoscale organization of NiV-M on the plasma membrane.** We conducted quantitative analyses of NiV-M clustering in WT and I349A using DBSCAN. The analysis covered various aspects: Total average density (TAD) is calculated by dividing the total number of molecules within an ROI by its size (A), Cluster diameter is measured in nm (B), Percentage of molecules in clusters (%) (C), Relative density within clusters

is calculated dividing the cluster density by the total density of ROI (TAD) (D), Circularity (E) and Hopkins index (F). For the study, we selected 16 WT cells, 9 I349A PK13 cells, and 14 K351 cells for DBSCAN analysis. Within each cell, we selected 10-20 ROIs. The p-values were determined using an unpaired student t test with Welch's correction: ns  $p > 0.05$ , \* $P \leq 0.05$ , \*\*  $P \leq 0.01$ , \*\*\*  $P \leq 0.001$ , \*\*\*\*  $P \leq 0.0001$ .

#### **4.5 Latrunculin A alters the nanoscale organization of NiV-M.**

Subsequently, we aimed to determine whether Latrunculin A, an actin depolymerizing drug, could induce alterations in NiV-M nano-organization similar to the effects observed with the I349A mutant. Once again, PK13 cells were employed, transfected with the WT NiV-M plasmid tagged with GFP. Prior to fixing the samples for SMLM imaging, they were treated with 1  $\mu$ M of LatA for 5 minutes or 1  $\mu$ M DMSO, as detailed in the *Materials and Methods* section. To visualize NiV-M assembly sites at the plasma membrane, the cells were permeabilized and stained with Alexa Fluor 47, following the same staining protocol as for the I349A and WT samples. The reconstructed images provided for each sample represent selected cells from a pool of DMSO-treated cells (9 cells) and LatA-treated cells (10 cells). Reconstructed images are displayed in panels A (Fig. 17). Within the reconstructed images, a yellow rectangle marks a region of interest (ROI) chosen for DBSCAN analysis. Approximately 10-20 ROIs were chosen per cell. Enlarged ROIs are presented in Figures 17B. The outcomes of the DBSCAN analysis are showcased as cluster maps, where unclustered NiV-M localizations are shown in gray, and clustered localizations are highlighted in red (Fig. 17C). Similarly, to the I349A mutant, LatA-treated cells have a higher count of unclustered NiV-M localizations than clusters compared to the DMSO control sample (Fig. 17C).

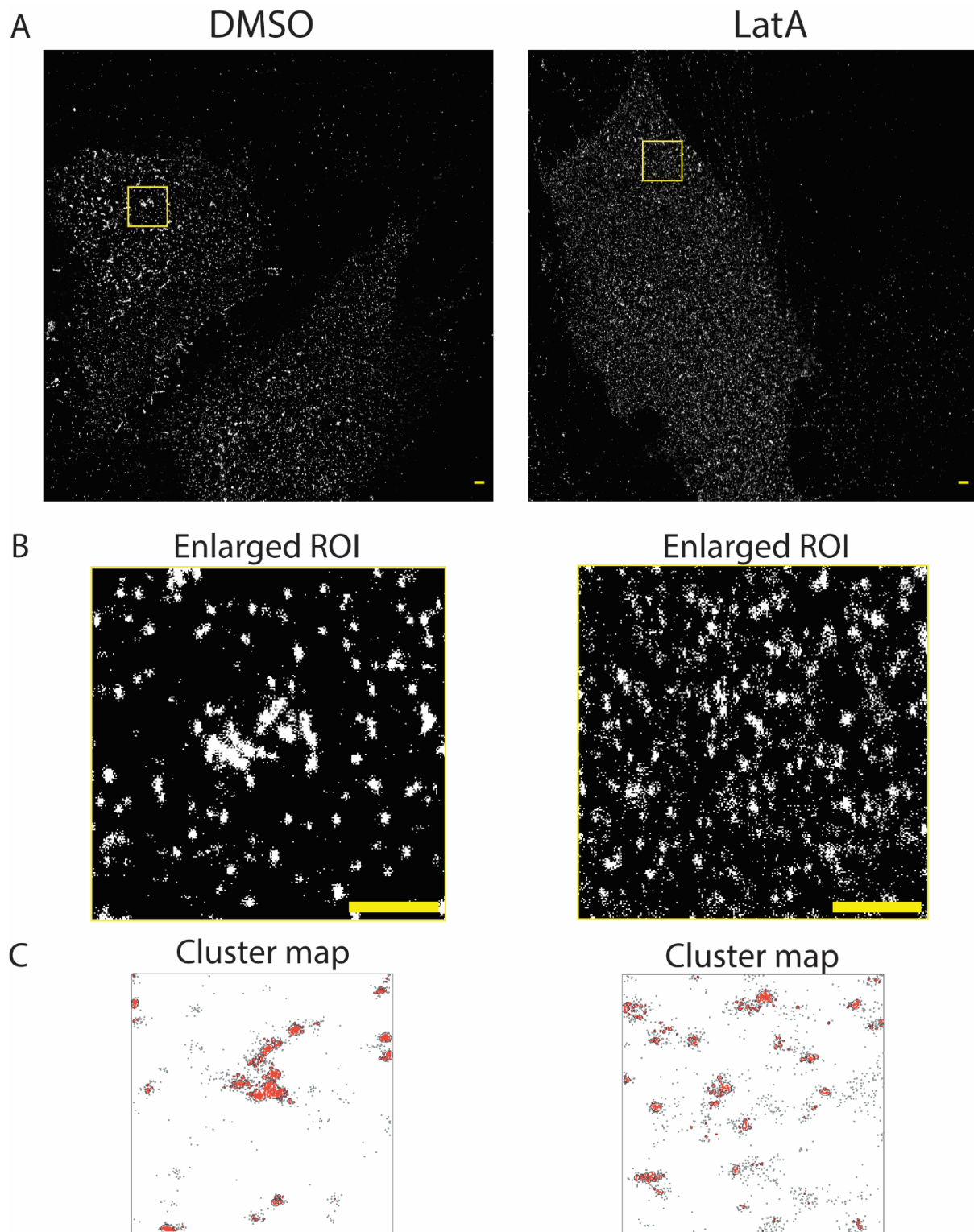


**Figure 17: The nano-organization of LatA-treated cells displays a distinct cluster pattern compared to control cells treated with DMSO. PK13 cells were transfected with NiV-M-GFP**

pcDNA3.1 constructs and treated with either 1  $\mu$ M of LatA for 5 minutes or 1  $\mu$ M DMSO. NiV-M was labeled using a rabbit anti-GFP antibody, followed by a donkey anti-rabbit antibody conjugated with Alexa Fluor 647 (A, D). Super-resolution images were captured using SMLM, and representative images were selected for each sample (A, D), including a cross-sectional view ( $\Delta z = 600$  nm). The scale bar measures 1  $\mu$ m. The region of interest (ROI) is highlighted within a yellow box in images B and E, which is then magnified to reveal the detailed distribution of NiV-M localizations. This detailed depiction provides insight into the specific arrangement of NiV-M. For the analysis, cluster analysis using DBSCAN was conducted on the magnified ROIs. Unclustered NiV-M localizations are displayed in gray, while clustered NiV-M localizations are highlighted in red on the cluster maps (C, F).

Subsequently, we followed a similar procedure as with I349A and WT. Implementing DBSCAN, we selected 10-20 ROIs per cell. The experiments were independently conducted twice, yielding 10 cells for LatA-treated and 9 cells for DMSO-treated samples. Our hypothesis suggested that actin would facilitate the formation of larger NiV-M arrays at the nanoscale on the plasma membrane. Thus, we speculated that actin depolymerization would yield results similar to those of the I349A mutant—dispersed NiV-M molecules. The percentage of molecules in clusters in DMSO-treated cells was significantly greater than LatA treated cells as expected (Figure 18A). This is also further confirmed through Hopkins analysis, DMSO demonstrated a higher cluster tendency of NiV-M localizations compared to LatA-treated cells (Figure 18B). As anticipated, LatA-treated cells exhibited smaller clusters compared to WT (Fig 18C). Surprisingly, LatA-treated cells displayed significantly rounder clusters compared to DMSO (Fig. 18D). The relative density and the total average density showed no significant difference between DMSO and LatA treatments (Fig. 18E, F). Given that both the TAD and relative density showed non-significant

values between DMSO and LatA-treated cells, this suggests that cluster density remains similar between them. Consequently, molecules are packed in a similar manner within clusters (Fig. 18E,F). In summary, the LatA-treated mutants displayed fewer clusters within selected ROIs, smaller clusters, and similar cluster density than the DMSO control cells—a pattern consistent with I349A and WT (Fig. 16). To make sure that the LatA treatment did not interfere with the localization of NiV-M at the plasma membrane, we used confocal microscopy (Figure 18G). The percentage of membrane localization was calculated using the ratio of GFP at the plasma membrane divided by the GFP intensity away from the membrane. The results show that the LatA treatment did not hinder NiV-M localization at the plasma membrane (Figure 18H).

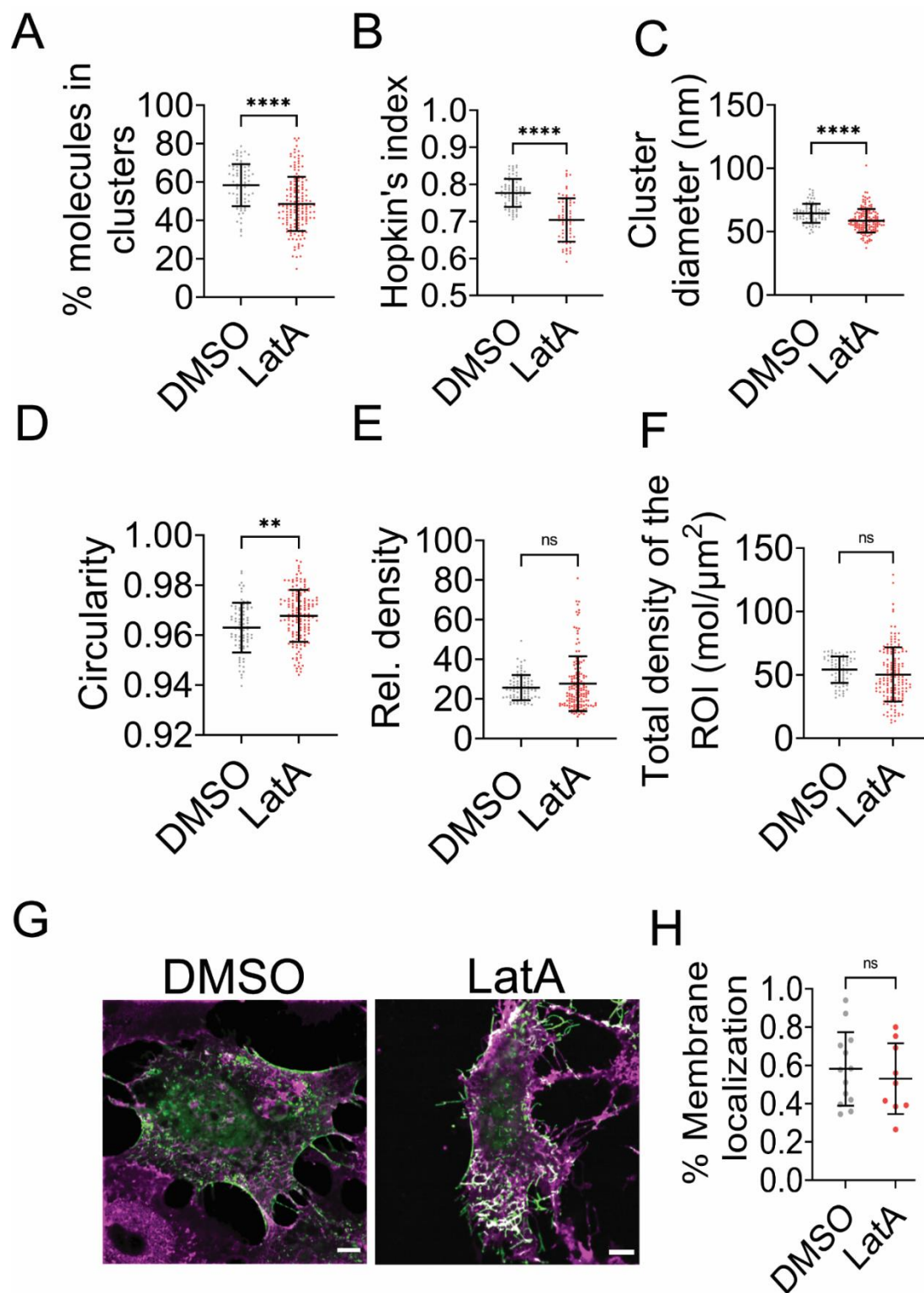


**Figure 18: LatA alters the nanoscale organization of NiV-M on the plasma membrane**

similarly to I349A. We conducted quantitative analyses of NiV-M clustering in LatA and DMSO

treated cells using DBSCAN. The analysis covered various aspects: Percentage of molecules in clusters (A), Hopkins index (B), Cluster diameter (C), Circularity (D), Relative density (E), Total density of the ROI ( $\text{mol}/\mu\text{m}^2$ ) (F). For the study, we selected 9 DMSO cells and 8 LatA cells for DBSCAN analysis. Within each cell, we selected 10-20 ROIs (A-F). PK13 cells were transfected with NiV-M-GFP (green) and their plasma membranes were stained with Alexa Fluor 647-conjugated wheat germ agglutinin (magenta) (G). Confocal microscopy was used to capture images, with a total of 13 cells treated with DMSO and 9 cells treated with LatA from three independent experiments. Representative images are presented in Figure G. The percentage of NiV-M membrane localization in DMSO and LatA-treated cells was determined by calculating the ratio of GFP fluorescence intensity at the plasma membrane to that of the entire cell (H). The p-values were determined using an unpaired student t test with Welch's correction: ns  $p > 0.05$ , \* $P \leq 0.05$ , \*\*  $P \leq 0.01$ , \*\*\*  $P \leq 0.001$ , \*\*\*\*  $P \leq 0.0001$ .

## 5. Discussion

### 5.1 The role of the putative actin-binding motif in NiV-M on virus assembly via actin interaction.

NiV-M plays a crucial role in both the assembly and budding of the virus [15]. This study delves into the discovery of a potentially pivotal actin-binding motif within the NiV-M C-terminal. Our results show that NiV-M-actin association is instrumental in the formation of larger assembly sites on a nanoscale at the plasma membrane, representing a vital step in preparing NiV for budding. The motif resembled a KLKK like motif and within this motif the isoleucine 349 (I349) was conserved across viral and actin-binding proteins, while lysine (K351) was exclusively conserved among viral proteins (Fig. 10). To better understand the significance of these conserved amino acids, we generated two KLKK mutants, replacing isoleucine (349) with alanine in one and lysine (351) with alanine in the other (Fig. 11). Our findings revealed a substantial reduction in NiV VLP budding in both mutants when compared to the wild type (WT), as confirmed through western blot analysis (Fig. 13). In pursuit of deeper insights, we explored the potential interaction between NiV-M and the actin cytoskeleton. Our experiments demonstrated an observable increase in  $\beta$ -actin in the cellular culture supernatant. This prompted us to conduct co-immunoprecipitation experiments to examine the protein expression levels of cellular NiV-M and  $\beta$ -actin (Fig.14). The results of these experiments indicated a clear interaction between NiV-M and  $\beta$ -actin in WT cells. As expected, the I349A mutation exhibited a weaker interaction compared to the WT. Surprisingly, the K351A mutant also showed reduced  $\beta$ -actin interaction, although to a lesser extent than the I349A mutant (Fig. 14). Nevertheless, even though the mutants displayed reduced budding compared to the WT, actin association was not entirely impaired, as evident from the immunoblot data (Figure 14). Therefore, our combined

data underscores that the I349A and K352A mutants do not fully inhibit actin interactions, as demonstrated by immunoblot assays against  $\beta$ -actin. This interaction persists, albeit at a decreased level, even within the VLPs compared to the WT samples (Figure 14). The enrichment of actin in VLPs was not surprising, as a previous proteomic study had already shown the incorporation of actin cytoskeleton factors in VLPs [22].

The significance of the I349A mutant becomes evident in our Single Molecule Localization Microscopy (SMLM) imaging experiments. Although more substantial changes can be achieved through deletions or double mutants, the I349A mutant's nanoscale organization resembled that of a sample treated with Latrunculin A (LatA). Our results revealed differences in assembly sites formed by the I349A and WT NiV-M. The former displayed smaller, sparser clusters with fewer molecules, while WT exhibited larger clusters with a higher molecule count. This intriguing differentiation at the nanoscale supports our hypothesis that the association between NiV-M and actin promotes the formation of larger nanoscale NiV-M arrays, priming them for effective budding. Conversely, the K351A mutant closely resembled the WT, with all statistical parameters being non-significant compared to the WT (Figure 16). While the K351A mutant exhibited reduced VLP production compared to the WT, it had no significant impact on the nanoscale organization of NiV-M at the plasma membrane. Therefore, our super-resolution microscopy analysis revealed distinct differences between the K351A and I349A mutant which was very surprising.

## **5.2 Comparing Isoleucine 349 and Lysine 351 in Actin Binding and Interaction**

The differences in nanoscale organization may be attributed to the unique properties of these amino acids and their conservation among actin-binding proteins. Isoleucine is hydrophobic and non-polar, meaning it prefers to interact with other hydrophobic substances [41]. In contrast,

lysine is a basic and positively charged amino acid, making it different in nature [41]. When we discuss actin binding, proteins that bind to actin typically interact with a specific hydrophobic region of actin. In this context, isoleucine's hydrophobic nature might make it better at binding to this part of actin or interacting with other proteins involved in actin interactions [42,43].

Therefore, mutating lysine to alanine might not significantly affect actin interaction because isoleucine, which may have a stronger interaction, was not mutated. Furthermore, the significance of isoleucine lies in its high degree of conservation among actin-binding proteins. A study conducted by Dominguez R. in 2016 involved the alignment of WH2 domains and WH2-related sequences among actin nucleators. Conservation scores were calculated for each amino acid based on this alignment. Notably, the isoleucine we mutated at position 349, which aligned within the IRQG of the WASP, was found to be highly conserved among actin nucleators [44]. This conservation suggests its likely important role for this interaction. Our co-immunoprecipitation results align with this hypothesis that the Isoleucine has a stronger effect upon the actin-interaction than the K351A mutant (Fig. 14).

### **5.3 Analyzing Latrunculin A (LatA) Effects on NiV-M-Actin Association**

In addition to showing a potential key amino acid for NiV-M-actin association we also investigated the NiV-M-actin interaction with our LatA experiments. Actin inhibitors, like LatA, have previously exhibited inhibitory effects on the late viral life cycle stages, including assembly and budding [45]. Our results reveal distinctions in assembly sites between LatA-treated and WT cells, characterized by smaller, sparser clusters with fewer molecules in LatA-treated cells. Conversely, WT cells or control DMSO treated cells displayed larger clusters with higher molecule counts. This intriguing differentiation at the nanoscale supports our hypothesis: the

association between NiV-M and actin facilitates the formation of bigger nanoscale NiV-M arrays, priming them for effective budding.

#### **5.4 The Actin cytoskeleton and NiV-M: Avenues for Further Research**

Together these experiments conducted on KLKK like motif and cells treated with LatA provided more insight on the NiV-M actin interaction during assembly and budding but there are still a lot of unanswered questions.

For example, to enhance our understanding of how NiV-M hijacks the actin cytoskeleton we could investigate whether it can modulate actin-related protein 2/3 (ARP2/3). For actin to form polymers, it relies on initiation complexes that secure its monomers. ARP2/3 stands as one such complex, and its activity can be increased by polymerization induction factors like WASP and WASP-interacting partners (WIPs). ARP2/3 initiation factor is favoured by many viruses [28]. For example, Respiratory syncytial virus (RSV) a paramyxovirus responsible for bronchiolitis and pneumonia in children under five years old worldwide modulates the actin-related protein 2/3 (ARP2/3). This interaction is important for its budding and cell-to-cell spread [46]. We could carry out further experiments using a drug called CK-666. CK-666 inhibits ARP2/3 by blocking its active conformational change [47]. Since NiV-M Proteomic based study has identified several important regulators of actin such as ARP2/3, testing CK-666 drug on cells infected with NiV-M would give us more insight on how NiV-M hijacks the actin cytoskeleton [15].

All our experiments exclusively used NiV-M without involving other proteins. It's possible that the actin cytoskeleton plays a role in NiV-M's interaction with other proteins. For instance, in the case of HIV budding assembly, the actin cytoskeleton is thought to drive interactions between the Gag and Envelope (Env) proteins [28]. As previously mentioned, the Measles M protein forms a

lattice beneath the plasma membrane, possibly acting as bridges between viral glycoproteins and the internal ribonucleocapsid containing the genetic material [21]. Dietzel, et al.'s study demonstrates that M-RNP transport to the plasma membrane occurs through actin filaments, essential for assembly at the plasma membrane [45]. It's conceivable that the VLPs budding from the mutants might lack the complete viral genetic information required for infecting another cell. However, due to our exclusive focus on NiV-M in our studies, this aspect remains unknown.

Moreover, our findings indicate that actin plays a role in promoting the assembly of larger nanoscale NiV-M arrays. The question remains: how exactly does the actin cytoskeleton contribute to the formation of these larger NiV-M arrays at the plasma membrane? One possibility is through its interaction with lipid rafts, which are specialized microdomains on the plasma membrane with distinct structural and functional properties. These dynamic and heterogeneous microdomains have diameters ranging from 10 to 200 nm, and although their existence was debated for years, the foundational chemical-physical properties of lipid-driven domains are now widely accepted [48]. The interaction between the actin cytoskeleton and lipid rafts needs to be investigated. Lipid rafts have demonstrated their pivotal role in various virus lifecycles. Notably, the severe acute respiratory syndrome coronavirus 2 (SARS-CoV-2) targets lipid rafts to enter host cells and facilitate budding [49]. Similarly, the Human Immunodeficiency Virus Type 1 (HIV-1) predominantly buds off through lipid rafts [50]. The interplay between the actin cytoskeleton and lipid rafts is significant; actin can influence the stability and dimensions of these lipid domains. For instance, during lymphocyte polarization, the actin cytoskeleton orchestrates membrane reorganization and the assembly of membrane rafts. This dynamic exchange between the actin cytoskeleton and rafts is crucial for raft stabilization and lymphocyte polarization [51]. The potential association between NiV-M and actin might be necessary for

plasma membrane reorganization involving lipid rafts, which could serve as platforms for assembly and budding. Studying these lipid rafts might also help us understand how the actin cytoskeleton could contribute to the formation of larger NiV-M arrays at the plasma membrane.

### **5.5 Targeting the NiV-M-Actin Interaction for New Antiviral Therapies**

All together our data demonstrates the importance of NiV-M-actin association for assembly and budding. The KLKK provides more insight into how NiV-M would interact with actin. This research is a big stepping stone into understanding the underlying biology necessary for development of antiviral drugs. Indeed, using actin inhibitors as anti-viral treatments has been demonstrated to be effective. For example, the small molecule Y-27632 inhibits the RHO-ROCK pathway and successfully block metastasis of Human Papillomavirus (HPV)-transformed cervical cancers. Therefore, viral-actin interactions can be targeted for new antiviral therapies and with more studies for NiV interaction with actin cytoskeleton specific compound can be used as a treatment [28].

### **5.6 Our Discovery of the PxxP Motif and Its Significance in Paramyxovirus Biology**

In addition to the previously identified KLKK motif, our research has uncovered another intriguing motif within the NiV-M C-terminal. While aligning paramyxoviruses and actin-binding proteins, we identified a highly conserved motif, PxxP. This discovery prompted us to conduct a series of experiments aimed at understanding its role in viral budding. We evaluated the cellular and VLP expression of two mutants, P328AP332A and P328A( $\Delta$ S)P332A, with fascinating results. Notably, none of the PxxP mutants displayed a band on the western blot for VLP, strongly suggesting the crucial involvement of this motif in NiV budding (Fig. 13).

Further investigation into the existing literature revealed that this motif is also referred to as the P(T/S)AP motif and is highly conserved among paramyxoviruses. Specifically, residues P329 and P332 are shared by several related viruses, including Hendra virus (HeV), Nipah virus (NiV), Hemagglutinin - Tupaia paramyxovirus (TPMV), Measles virus (MeV), and Sendai virus (SeV) [52].

### **5.7 Understanding the Role of the PxxP Motif in Budding**

It's important to note that our discovery is not the first to suggest a connection between this motif and viral budding. Research led by Patch, J. R. et al., have proposed that this motif could function as an L-domain amino acid motif. L-domains are crucial for the budding of enveloped viruses as they interact with host proteins to ensure efficient viral release. In the case of NiV, these researchers have postulated three potential L-domain amino acid motifs: P(T/S)AP (329-332), PPxY (29-39), and YP(x)nL (92-97), with the P(T/S)AP motif being the one we identified and subsequently mutated. However, none of these motifs have yet been confirmed as L-domains in NiV-M [52].

Our research strongly indicates that the PxxP motif plays a crucial role in viral budding, a hypothesis supported by the work of Patch, et al., who suggest that it could be a potential L-domain. The mechanism underlying the inhibition of budding in the absence of this motif may be related to the failure to recruit the necessary cellular machinery for the fission of viral buds [52].

Research by Kaneko T, et al. unveiled that the vesicular stomatitis virus (VSV) encodes a PPPY and PSAP motifs within its M protein [53]. By mutating the two prolines from the PxxP motifs to alanine, Kaneko T, et al. observed impaired SH3 domain binding. Further research in the case of VSV discovered that the PxxP motif directly interacts with tsg101, an ESCRT-I component in

mammalian cells. This motif is also found in the HIV-Gag and is involved with interacting with tsg101 in host cells [39, 53]. Enveloped virus budding involves a fission event to liberate viral particles from the cell membrane. Due to the absence of packaged fusion machinery, HIV relies on cellular fission machinery. The "PTAP" motif has emerged as a potential docking site for recruiting this machinery in HIV, potentially binding to host cellular factors [54]. ESCRT machinery is very important for viral budding since it is responsible for fission and viral release [55].

Considering the publications mentioned, a hypothesis emerges that the inability of the P328AP332A mutant to facilitate viral budding may be attributed to its failure to bind and recruit the ESCRT machinery. Although this hypothesis requires further validation, it presents an opportunity for future research, potentially utilizing the SMLM microscope for dual-color imaging with 10 nm resolution to determine whether the ESCRT machinery colocalizes with NiV-M in WT versus mutant samples. However, it's important to note that the viability of the deletion mutant P328A( $\Delta$ S)P332A remains uncertain due to its potential for reduced expression compared to WT, resulting in less cell lysate available for immunoblotting. In conclusion, the PxxP motif holds promise as a crucial L-domain, deserving further exploration and investigation.

## 6. Conclusion:

In conclusion, our study has brought to light the pivotal role of NiV-M in both the assembly and budding of the Nipah virus [15]. We've delved into the discovery of a potentially crucial actin-binding motif within the NiV-M C-terminal. Our results demonstrate that the NiV-M-actin association plays a critical role in the formation of larger assembly sites on a nanoscale at the plasma membrane, representing a vital step in preparing NiV for budding. This motif, resembling a KLKK-like sequence, is of significant interest [27].

Our research focused on the KLKK-like motif mutants, as they were believed to possess actin-binding capabilities [27]. Indeed, in comparison to the wild-type, KLKK mutants showed reduced actin incorporation into VLPs. The results of co-immunoprecipitation experiments indicated a clear interaction between NiV-M and  $\beta$ -actin in WT cells. As expected, the I349A mutation exhibited a weaker interaction compared to the WT. Furthermore, by using Single-Molecule Localization Microscopy (SMLM) imaging, we demonstrated that mutations within the KLKK-like motif influenced the nanoscale organization of NiV-M at the plasma membrane. Specifically, the I349A mutant displayed smaller, sparser clusters with fewer molecules per cluster than the wild-type. Interestingly, treatment with the actin depolymerization drug Latrunculin A yielded a similar nanoscale organization to that of the I349A mutant, characterized by smaller clusters with fewer molecules. We also proposed an explanation on why the K351A mutation did not alter the nanoscale organization of NiV-M at the plasma membrane. We suggest that Isoleucine has a stronger effect on the actin interaction than the K351A mutant, which aligns with our co-immunoprecipitation data [41, 42, 44].

Despite the insights gained through this study, several unanswered questions remain. Further investigations could explore how NiV-M modulates actin-related protein 2/3 (ARP2/3), a crucial

component in actin polymerization. Additionally, exploring the interplay between the actin cytoskeleton and lipid rafts could provide further insights into the formation of larger NiV-M arrays at the plasma membrane [46, 47, 48, 49, 50, 51].

Our second discovery of the PxxP motif within the NiV-M C-terminal has unveiled an intriguing and highly conserved element in paramyxoviruses with significant implications for viral budding [52]. Our experiments, which involved mutating this motif, strongly suggest its crucial involvement in NiV budding. This finding aligns with previous research proposing it as a potential L-domain amino acid motif, essential for efficient viral release [52, 53].

In view of these findings, targeting the NiV-M-actin interaction for the development of new antiviral therapies is a promising avenue. Actin inhibitors have shown effectiveness in combating viral infections, and further research into NiV's interaction with the actin cytoskeleton may lead to specific compounds for treatment [28]. As for the PxxP motif, it presents itself as a promising candidate for a crucial L-domain in paramyxovirus biology, deserving further exploration and in-depth investigation in the field of virology.

This research serves as a significant step in unraveling the underlying biology necessary for the development of antiviral drugs. The potential for these findings to lead to novel antiviral therapies is promising, and further research will undoubtedly expand our understanding of this critical aspect of virus assembly and budding.

## 7. References:

1. MacLachlan, N. J., & Dubovi, E. J. (2017). Chapter 17 - Paramyxoviridae and Pneumoviridae. In *Elsevier Fenner's Veterinary Virology* (Fifth Edition) (pp. 327-356).
2. World Health Organization. (2023). Measles. Retrieved from <https://www.who.int/news-room/fact-sheets/detail/measles>.
3. Thibault, P. A., Watkinson, R. E., Moreira-Soto, A., Drexler, J. F., & Lee, B. (2017). Chapter One - Zoonotic Potential of Emerging Paramyxoviruses: Knowns and Unknowns. In *Advances in Virus Research*, pp. 1–55. <https://doi.org/10.1016/bs.aivir.2016.12.001>.
4. Drexler, J. F., Corman, V. M., Müller, M. A., Maganga, G. D., Vallo, P., Binger, T., ... Drosten, C. (2012). Bats host major mammalian paramyxoviruses. *Nature Communications*, 3, 796. <https://doi.org/10.1038/ncomms1796>.
5. Aguilar, H. C., Henderson, B. A., Zamora, J. L., & Johnston, G. P. *In Press*. Current Clinical Microbiology Reports. <https://doi.org/10.1007/s40588-016-0040-8>.
6. Wang, L. F., Mackenzie, J. S., & Broder, C. C. (2013). Henipaviruses. In D. M. Knipe & P. M. Howley (Eds.), *Fields virology* (6th ed., pp. 286–313). Lippincott Williams & Wilkins.
7. Ang, B. S. P., Lim, T. C. C., & Wang, L. (2018). Nipah Virus Infection. *American Society for Microbiology*, 56(6). <https://doi.org/10.1128/jcm.01875-17>.
8. Centers for Disease Control and Prevention. (February 2, 2023). Nipah virus outbreak distribution map. Retrieved from <https://www.cdc.gov/vhf/nipah/outbreaks/distribution-map.html>.
9. World Health Organization. (2023). Nipah virus infection - Bangladesh. Retrieved from <https://www.who.int/emergencies/disease-outbreak-news/item/2023-DON442>.
10. Conroy, G. (2023, September 22). Nipah virus outbreak: What scientists know so far. *Nature*. <https://www.nature.com/articles/d41586-023-02967>.
11. World Health Organization. (2023). Nipah Virus Outbreak in Kerala. Retrieved from <https://www.who.int/southeastasia/outbreaks-and-emergencies/health-emergency-information-risk-assessment/surveillance-and-risk-assessment/nipah-virus-outbreak-in-kerala>.

12. World Health Organization. (2021). R&D Blueprint and Nipah Virus. Retrieved from <https://www.who.int/teams/blueprint/nipah>.
13. Centers for Disease Control and Prevention. (2020, October 6). Nipah virus transmission. Retrieved from <https://www.cdc.gov/vhf/nipah/transmission/index.html>.
14. Chattu, V. K., et al. (2018). Nipah Virus epidemic in Southern India and emphasizing 'One Health' approach to ensure global health security. *Journal of Family Medicine and Primary Care*, 7, 275-283. [https://doi.org/10.4103/jfmpe.jfmpe\\_137\\_18](https://doi.org/10.4103/jfmpe.jfmpe_137_18).
15. Watkinson, R. E., & Lee, B. (2016). Nipah virus matrix protein: expert hacker of cellular machines. *FEBS Letters*, 590(15), 2494–2511. <https://doi.org/10.1002/1873-3468.12272>.
16. Matveeva, O. V., Guo, Z. S., Shabalina, S. A., & Chumakov, P. M. (2015). Oncolysis by paramyxoviruses: multiple mechanisms contribute to therapeutic efficiency. *Molecular Therapy - Oncolytics*, 2, 15011. <https://doi.org/10.1016/bs.aivir.2016.12.001>.
17. Thibault, P. A., Watkinson, R. E., Moreira-Soto, A., Drexler, J. F., & Lee, B. (2017). Chapter One - Zoonotic Potential of Emerging Paramyxoviruses: Knowns and Unknowns. In *Advances in Virus Research*, pp. 1–55. <https://doi.org/10.1016/bs.aivir.2016.12.001>.
18. Hauser, N., Gushiken, A. C., Narayanan, S., Kottlilil, S., & Chua, J. V. (2021). Evolution of Nipah Virus Infection: Past, Present, and Future Considerations. *Tropical Medicine and Infectious Disease*, 6, 24. <https://doi.org/10.3390/tropicalmed6010024>.
19. Norris, M. J., Husby, M. L., Kiosses, W. B., Yin, J., Saxena, R., Rennick, L. J., ... Sapphire, E. O. (2022). Measles and Nipah virus assembly: Specific lipid binding drives matrix polymerization. *Science Advances*, 8(29), eabn1440. <https://doi.org/10.1126/sciadv.abn1440>.
20. Nooraei, S., Bahrulolum, H., Hoseini, Z. S., et al. (2021). Virus-like particles: preparation, immunogenicity and their roles as nanovaccines and drug nanocarriers. *Journal of Nanobiotechnology*, 19, 59. <https://doi.org/10.1186/s12951-021-00806-7>.
21. Ke, Z., Strauss, J. D., Hampton, C. M., Brindley, M. A., Dillard, R. S., Leon, F., ... Wright, E. R. (2018). Promotion of virus assembly and organization by the measles virus matrix protein. *Nature Communications*, 9. <https://doi.org/10.1038/s41467-018-04058-2>.

22. Johnston, G. P., Bradel-Tretheway, B., Piehowski, P. D., Brewer, H. M., Lee, B. N. R., Usher, N. T., ... Aguilar, H. C. (2019). Nipah Virus-Like Particle Egress Is Modulated by Cytoskeletal and Vesicular Trafficking Pathways: a Validated Particle Proteomics Analysis. *mSystems*, 4. <https://doi.org/10.1128/msystems.00194-19>.
23. Tyrrell, D. L. J., & Norrby, E. (1978). Structural polypeptides of measles virus. *Journal of General Virology*, 39, 219–229. <https://doi.org/10.1099/0022-1317-39-2-219>.
24. Bohn, W., Rutter, G., Hohenberg, H., Mannweiler, K., & Nobis, P. (1986). Involvement of actin filaments in budding of measles virus: studies on cytoskeletons of infected cells. *Virology*, 149, 91–106. <https://doi.org/10.1186/1743-422X-10-249>.
25. Stallcup, K. C., Raine, C. S., & Fields, B. N. (1983). Cytochalasin B inhibits the maturation of measles virus. *Virology*, 124, 59–74. [https://doi.org/10.1016/0042-6822\(83\)90290-8](https://doi.org/10.1016/0042-6822(83)90290-8).
26. Fagraeus, A., Tyrrell, D. L. J., Norberg, R., & Norrby, E. (1978). Actin filaments in paramyxovirus-infected human fibroblasts studied by indirect immunofluorescence. *Archives of Virology*, 296, 291–296. <https://doi.org/10.1007/BF01320068>.
27. Takimoto, T., Murti, K. G., Bousse, T., Scroggs, R. A., & Portner, A. (2001). Role of matrix and fusion proteins in budding of Sendai virus. *Journal of Virology*, 75(23), 11384–11391. <https://doi.org/10.1128/JVI.75.23.11384-11391.2001>.
28. Taylor, M., Koyuncu, O., & Enquist, L. (2011). Subversion of the actin cytoskeleton during viral infection. *Nature Reviews Microbiology*, 9, 427–439. <https://doi.org/10.1038/nrmicro2574>.
29. Sauer, M., & Heilemann, M. (2017). Single-Molecule Localization Microscopy in Eukaryotes. *Chemical Reviews*, 117(11), 7478–7509. <https://doi.org/10.1021/acs.chemrev.6b00667>.
30. Liu, Q., Chen, L., Aguilar, H. C., Chou, K. C. (2018). A stochastic assembly model for Nipah virus revealed by super-resolution microscopy. *Nature Communications*, 9. <https://doi.org/10.1038/s41467-018-05480-2>.

31. Lelek, M., Gyparaki, M. T., Beliu, G., Schueder, F., Griffié, J., Manley, S., ... Zimmer, C. (2021). Single-molecule localization microscopy. *Nature Reviews Methods Primers*, 1. <https://doi.org/10.1038/s43586-021-00038-x>.
32. Mirsalehi, M. M. (2003). Optical Information Processing. In *Encyclopedia of Physical Science and Technology* (3rd ed., pp. 335–369). Academic Press. <https://doi.org/10.1016/B0-12-227410-5/00525-1>.
33. Von Diezmann, L., Shechtman, Y., & Moerner, W. E. (2017). Three-Dimensional Localization of Single Molecules for Super-Resolution Imaging and Single-Particle Tracking. *Chemical Reviews*, 117(11), 7244–7275. <https://doi.org/10.1021/acs.chemrev.6b00629>.
34. Pagoon, S. V., Nicovich, P. R., Mollazade, M., Tabarin, T., & Gaus, K. (2016). Clus-DoC: a combined cluster detection and colocalization analysis for single-molecule localization microscopy data. *Molecular Biology of the Cell*, 27(22), 3627–3636. <https://doi.org/10.1091/mbc.E16-07-0478>.
35. Pagoon, S. V., Tabarin, T., Yamamoto, Y., Ma, Y., Nicovich, P. R., Bridgeman, J. S., ... Gaus, K. (2016). Functional role of T-cell receptor nanoclusters in signal initiation and antigen discrimination. *Proceedings of the National Academy of Sciences*, 113(37), E5454-E5463. <https://doi.org/10.1073/pnas.1607436113>.
36. Rojek, J. M., Perez, M., & Kunz, S. (2008). Cellular Entry of Lymphocytic Choriomeningitis Virus. *Journal of Virology*, in press. <https://doi.org/10.1128/jvi.01331-07>.
37. Tafteh, R., Scriven, D. R., Moore, E. D., & Chou, K. C. (2016). Single molecule localization deep within thick cells; a novel super - resolution microscope. *Journal of Biophotonics*, 9, 155 – 160. <https://doi.org/10.1002/jbio.201500140>.
38. Wang, Y. E., Park, A., Lake, M., Pentecost, M., Torres, B., Yun, T. E., ... Lee, B. (2010). Ubiquitin-Regulated Nuclear-Cytoplasmic Trafficking of the Nipah Virus Matrix Protein Is Important for Viral Budding. *PLOS Pathogens*, 6, e1001186. <https://doi.org/10.1371/journal.ppat.1001186>.

39. Kaneko, T., Li, L., & Li, S. S. (2008). The SH3 domain--a family of versatile peptide- and protein-recognition module. *Frontiers in Bioscience*, *13*, 4938–5252. <https://doi.org/10.2741/3053>.
40. Ester, M., Kriegel, H. P., Sander, J., & Xu, X. (1996). A density-based algorithm for discovering clusters in large spatial databases with noise. In Proceedings of the 2nd International Conference on Knowledge Discovery and Data Mining (pp. 226–231). AAAI.
41. Betts, M. J., & Russell, R. B. (2003). Amino acid properties and consequences of substitutions. In *Bioinformatics for Geneticists* (M. R. Barnes & I. C. Gray, Eds.), Wiley.
42. Kathuria, S. V., Chan, Y. H., Nobrega, R. P., Özen, A., & Matthews, C. R. (2016). Clusters of isoleucine, leucine, and valine side chains define cores of stability in high-energy states of globular proteins: Sequence determinants of structure and stability. *Protein Science*, *25*(3), 662–675. <https://doi.org/10.1002/pro.2860>.
43. Carlier, M., Pernier, J., & Avvaru, B. S. (2013). Control of Actin Filament Dynamics at Barbed Ends by WH2 Domains: From Capping to Permissive and Processive Assembly. *Cytoskeleton*, *70*, 540–549. <https://doi.org/10.1002/cm.21124>.
44. Dominguez, R. (2016). The WH2 Domain and Actin Nucleation: Necessary but Insufficient. *Trends in Biochemical Sciences*, *41*(6), 478–490. <https://doi.org/10.1016/j.tibs.2016.03.004>.
45. Dietzel, E., Kolesnikova, L., & Maisner, A. (2013). Actin filaments disruption and stabilization affect measles virus maturation by different mechanisms. *Virology Journal*, *10*, 249. <https://doi.org/10.1186/1743-422X-10-249>.
46. Paluck, A., Osan, J., Hollingsworth, L., Talukdar, S. N., Saegh, A. A., & Mehedi, M. (2021). Role of ARP2/3 Complex-Driven Actin Polymerization in RSV Infection. *Pathogens (Basel, Switzerland)*, *11*(1), 26. <https://doi.org/10.3390/pathogens11010026>.
47. Hetrick, B., Han, M. S., Helgeson, L. A., & Nolen, B. J. (2013). Small molecules CK-666 and CK-869 inhibit actin-related protein 2/3 complex by blocking an activating conformational change. *Chemistry & Biology*, *20*(5), 701–712. <https://doi.org/10.1016/j.chembiol.2013.03.019>.

48. Levental, I., Levental, K. R., & Heberle, F. A. (2020). Lipid Rafts: Controversies Resolved, Mysteries Remain. *Trends in Cell Biology*, 30(5), 341–353. <https://doi.org/10.1016/j.tcb.2020.01.009>.
49. Roncato, R., Angelini, J., Pani, A., Talotta, R. (2022). Lipid rafts as viral entry routes and immune platforms: A double-edged sword in SARS-CoV-2 infection? *Biochimica et Biophysica Acta (BBA) - Molecular and Cell Biology of Lipids*, 1867(6), 159140. <https://doi.org/10.1016/j.bbalip.2022.159140>.
50. Nguyen, D. H., & Hildreth, J. E. (2000). Evidence for budding of human immunodeficiency virus type 1 selectively from glycolipid-enriched membrane lipid rafts. *Journal of Virology*, 74(7), 3264–3272. <https://doi.org/10.1128/jvi.74.7.3264-3272.2000>.
51. Viola, A., & Gupta, N. (2007). Tether and trap: Regulation of membrane-raft dynamics by actin-binding proteins. *Nature Reviews Immunology*, 7, 889–896. <https://doi.org/10.1038/nri2193>.
52. Patch, J. R., Han, Z., McCarthy, S. E., Yan, L., Wang, L. F., Harty, R. N., & Broder, C. C. (2008). The YPLGVG sequence of the Nipah virus matrix protein is required for budding. *Virology Journal*, 5, 137. <https://doi.org/10.1186/1743-422X-5-137>.
53. Irie, T., & Harty, R. N. (2005). L-Domain Flanking Sequences Are Important for Host Interactions and Efficient Budding of Vesicular Stomatitis Virus Recombinants. *Journal of Virology*, 79(20), 12617–12622. <https://doi.org/10.1128/jvi.79.20.12617-12622.2005>.
54. Garrus, J. E., von Schwedler, U. K., Pornillos, O. W., Rich, R. L., Myszka, D. G., & Sundquist, W. I. (2001). Tsg101 and the Vacuolar Protein Sorting Pathway Are Essential for HIV-1 Budding. *Cell*, 107(1), 55–65. [https://doi.org/10.1016/S0092-8674\(01\)00506-2](https://doi.org/10.1016/S0092-8674(01)00506-2).
55. Votteler, J., & Sundquist, W. I. (2013). Virus budding and the ESCRT pathway. *Cell Host & Microbe*, 14(3), 232–241. <https://doi.org/10.1016/j.chom.2013.08.012>.